https://doi.org/10.5194/essd-2026-627
Preprint. Discussion started: 19 August 2026

Open Access Earth System Science Data Discussions

Revisiting Sea-level and global water budgets for the period 1993-2022 within ESA Climate change initiative

Alejandro Blazquez[1], Benoit Meyssignac[1], Robin Fraudeau[2], Michael Ablain[2], Jonathan Bamber[3], Antonio Bonaduce[4], Marie Bouih[2], Anny Cazenave[2], Thorben Döhne[5], Ines Dussaillant[6], Ramiro Ferrari[2], Martin Horwath[5], Nicolas Kolodziejczyk[7], Hugo Lecomte[1,8], Stephanie Leroux[9], William Llovel[7], Daniele Melini[10], Erwan Oulhen[7], Thierry Penduff[11], Roshin P. Raj[4], Giorgio Spada[12], Marius Schlaak[1], Papasarafianou Stamatia[13], Andrea Storto[13], Chunxue Yang[13], and Sarah Connors[14]

[1]Université de Toulouse, LEGOS (CNES/CNRS/IRD/UT), Toulouse, France
[2]Magellium, Toulouse, France
[3]University of Bristol, Bristol, UK, Institute for Advanced Study, Technical University Munich, Germany
[4]Nansen Environmental and Remote Sensing Center, Bergen, Norway
[5]TUD Dresden University of Technology, Dresden, Germany
[6]Universidad de Chile Center for Mathematical Modeling, Santiago, Chile
[7]Univ Brest, CNRS, Ifremer, IRD, Laboratoire d'Océanographie Physique et Spatiale (LOPS), IUEM, Plouzané, France.
[8]Finnish Geospatial Research Institute, National Land Survey of Finland, Espoo, Finland
[9]DATLAS, Grenoble, France
[10]Istituto Nazionale di Geofisica e Vulcanologia, Roma, Italy
[11]Université Grenoble Alpes, CNRS, INRAE, IRD, Grenoble INP, Institut des Géosciences de l'Environnement (IGE), Grenoble, France
[12]University of Bologna, Bologna, Italy
[13]Institute of Marine Science, National Research Council of Italy, Rome, Italy
[14]European Space Agency, Climate Office, Oxfordshire, UK

Correspondence: Alejandro Blazquez (alejandro.blazquez@cnes.fr)

Abstract. Sea-level rise, driven by anthropogenic greenhouse-gas forcing, is one of the best indicators of climate change. Satellite altimetry, the global Argo profiling network, and space-borne gravimetry (GRACE/GRACE-FO) have enabled quantitative monitoring of the sea-level budget, yet recent analyses reveal a persistent non-closure after 2015. We present an updated assessment of the global and regional sea-level budget for the satellite era (1993–2022), extending the previous ESA-CCI evaluation with refined uncertainty characterisation and an objective inverse closure framework. Global-mean sea-level (GMSL) trend and associated uncertainties at 90% confidence level are accelerating from $3.39 \pm 0.20\ mm\ yr^{-1}$ for 1993–2022 to $3.86 \pm 0.18\ mm\ yr^{-1}$ for 2004–2022. GMSL is driven primarily by land-ice mass loss of $1.44 \pm 0.09\ mm\ yr^{-1}$ and $1.74 \pm 0.09\ mm\ yr^{-1}$, respectively, alongside the thermosteric contribution of $1.24 \pm 0.14\ mm\ yr^{-1}$ and $1.32 \pm 0.15\ mm\ yr^{-1}$, for the same periods. The budget closes robustly until 2015 with residuals under $0.3\ mm\ yr^{-1}$ (less than 10% of the trend). Thereafter a statistically significant residual trend emerges, independent of the barystatic sea-level either from gravimetry or via the global water budget, indicating either a systematic inconsistency or multiple single-dataset artifact.

Regional analysis identifies persistent non-closure in the North Atlantic, around Australia, and to a lesser extent in the North Pacific—patterns that resemble the largest steric signals and suggest underestimation of deep-ocean steric contributions or

https://doi.org/10.5194/essd-2026-627
Preprint. Discussion started: 19 August 2026

overestimation of altimetric sea-level. An objective weighted-least-squares inversion (applicable from 2004 onward) demonstrates that a closed solution exists within combined uncertainties for 2004–2016, but closure fails at the 1σ level from 2017 onward, with less than 32% probability of consistency. The inversion requires modest adjustments to satellite altimetry but substantial corrections to the gravimetric mass term, suggesting the GRACE-FO transition as a likely source of the budget breakdown.

These findings highlight the need for improved deep-ocean observations, refined gravimetric processing, and spatial error-correlation estimates to achieve reliable sea-level budget closure at regional scales in the continued satellite era.

Short summary Closing the sea-level budget on annual and longer time scales is a cornerstone of physical oceanography because sea-level rise is one of the clearest, most direct indicators of anthropogenic climate change, and a closed budget shows we have identified and quantified all major drivers. We examined the global sea-level budget from 1993 to 2022, finding an accelerated rise that matched ice melt and warm water until 2015. After 2015 a small unexplained gap appears, likely from changes in gravity measurements. Better deep-ocean observations and refined gravity processing are needed to close the budget.

1 Introduction

Anthropogenic greenhouse gas emissions since the industrial era have altered the optical depth of atmospheric layers to infrared radiation, perturbing the radiative response of the Earth to incoming solar radiation and inducing a radiative imbalance at the top of the atmosphere. The Earth now absorbs more energy than it emits towards space and is therefore accumulating heat. Most of this energy is stored as enthalpy in the ocean, leading to the thermal expansion of seawater and thus to sea-level rise. Part of this energy is absorbed by land ice, causing it to melt and contributing further to sea-level rise. The resulting rapid increase in sea-level threatens coastal communities and ecosystems worldwide, making sea-level rise one of the most concerning consequences of climate change.

Thanks to the large network of tide gauges operating along the world's coastlines throughout the 20th century, Church and White (2006) were able to detect a rapid sea-level rise of $1.7 \pm 0.3\ mm\ yr^{-1}$. However, the precise quantification of sea-level rise has always been challenging, because tide gauges are sparsely and unevenly distributed along the world's coastlines, because they are subject to vertical land motion that locally masks the effect of anthropogenic sea-level rise on relative sea-level, and because they do not sample the open ocean,whose variability in SLR can differ significantly compared to the coastal zone (Leclercq et al., 2025), leading to low confidence in global sea-level rise estimates.

Since then, the climate science community has worked continuously to understand the causes of the current rapid sea-level rise, the observed acceleration, the regional disparities in rates and acceleration, and how these connect to anthropogenic GHG emissions.

A central tool in this endeavour has been the testing of sea-level budget closure. This approach originates from the seminal discussion by Munk and Revelle (1952), who attempted to account for the sea-level rise observed by tide gauges by summing contributions from glaciers and ocean thermal expansion. The approach became systematic from the 1990s onwards, as authors sought to attribute the observed rapid sea-level rise to the estimated contributors: thermal expansion, glaciers, and ice sheets,

https://doi.org/10.5194/essd-2026-627
Preprint. Discussion started: 19 August 2026

which consistently fell short of the observed rise from satellite altimetry. This gap drove much of the subsequent research. Warrick and Oerlemans (1990), in the IPCC First Assessment Report, provided one of the first systematic multi-contributor budget assessments at the community level.

The early 2000s saw two major advances in the ocean observing system that proved transformative for sea-level budget studies. The first was the deployment of the global Argo array of autonomous profiling floats, which for the first time enabled continuous, quasi-global monitoring of ocean temperature and salinity down to $2\,000\ m$ depth, with high precision and accuracy validated against conductivity–temperature–depth (CTD) systems. Although the array comprises only a few thousand point-wise profilers, it achieved sufficient spatial coverage by 2005 to provide robust estimates of global ocean thermal expansion and the associated sea-level contribution. The second advance was the launch of the Gravity Recovery and Climate Experiment (GRACE) mission, whose space gravimetry measurements enabled the detection of mass transfers at the Earth's surface at interannual timescales with unprecedented precision (Tapley et al., 2004). By 2004, GRACE data quality was sufficient to quantify ocean mass changes and the associated sea-level contributions from land ice loss and land water storage changes. From 2005 onwards, the combined availability of Argo and GRACE data allowed researchers to partition sea-level changes into their steric and mass components, and to verify — through comparison with satellite altimetry — that their sum is consistent with total observed sea-level change within uncertainties. Closing the sea-level budget at annual and longer timescales thus became a central problem of modern physical oceanography, for three main reasons. First, it provides a means to verify, with high confidence, that all important causes of sea-level variability have been identified and that their combined effect matches the observed total change — in other words, it ensures a quantitative understanding of why and how sea-level is rising. Second, it serves as a cross-validation framework for the complex observing systems involved — the Argo network, the GRACE and GRACE-FO space gravimetry missions, and the satellite altimetry system — enabling the detection of instrument issues or long-term drifts by exploiting the built-in redundancy between independent observing pathways. Third, it provides an efficient means of testing the internal consistency of observed climate variables — sea-level, ocean temperature, and ocean mass — with respect to conservation laws of mass, energy, and freshwater, which is particularly important for constraining ocean reanalyses that must assimilate coherent data to satisfy the governing equations of ocean dynamics and thermodynamics.

Recent community studies (WCRP Global Sea Level Budget Group, 2018; Horwath et al., 2022) consistently demonstrate that the sea-level budget can be robustly closed over the satellite era up to 2016, from the early altimetry period (1993–2016) through the GRACE–Argo period (2005–2016), within uncertainties of approximately $0.3\ mm\ yr^{-1}$ ($< 10\%$ of the trend). These studies report highly consistent GMSL rise rates ($\sim 3.0 - 3.1\ mm\ yr^{-1}$ since 1993, increasing to $\sim\ 3.6\ mm\ yr^{-1}$ after the early 2000s) and identify a measurable acceleration ($\sim 0.1\ mm\ yr^{-2}$), primarily driven by increasing land ice mass loss, especially from Greenland. Thermal expansion and ocean mass contributions together explain the observed rise, with a broadly comparable partitioning (steric: $\sim 33 - 42\%$; mass: $\sim 57 - 66\%$), with glaciers and ice sheets dominating the mass term. Sea-level budget closure is achieved not only for long-term trends but also at interannual timescales, and even for monthly variability in the more recent datasets, demonstrating the internal consistency of satellite altimetry, the Argo network, and GRACE/GRACE-FO. Remaining discrepancies are small, well within the 1σ uncertainty level, localised in time, and largely attributable to uncertainties in land water storage or deep-ocean contributions.

https://doi.org/10.5194/essd-2026-627
Preprint. Discussion started: 19 August 2026

Open Access Earth System Science Data Discussions

Since 2017, however, the picture has changed substantially. Recent investigations have shown that beyond that date, sea-level budget is no longer close, with an inconsistency between the sum of contributors and the observed total that exceeds the 2σ uncertainty level (Barnoud et al., 2021, 2023a; Chen et al., 2020; Cazenave et al., 2026). This non-closure was initially suspected to stem from errors in the observational datasets, including a drift in the wet tropospheric correction applied to the Jason-3 altimetry mission due to a malfunction of the onboard radiometer (Barnoud et al., 2023a; Brown et al., 2023), a drift in the Argo salinity record (Barnoud et al., 2021) and instrumental problems in GRACE and GRACE-FO over this period (Barnoud et al., 2023b). However, after correction of these errors or assessment of their magnitude, they were found to be insufficient to explain the non-closure. Several studies have proposed different attributions as: (I) a significant deep-ocean contribution of $0.4 \pm 0.15\ mm\ yr^{-1}$ over 2005–2022, approximately 10% of the observed GMSL rise over that period (Cazenave et al., 2026) implying that the deep-ocean contribution to sea-level rise may be as much as four times larger than previously estimated by Purkey and Johnson (2010)on the order of $0.1\ mm\ yr^{-1}$ over the period from 1980 to 2010, (II) a GIA mismodelling of solid-Earth viscous deformation signals(Hightower et al., 2026preprint), and (III) missing solid-Earth deformation due the present-day water mass redistributions (Moreira et al., 2021)

This persistent non-closure of the sea-level budget since 2017 has renewed interest in the budget approach and motivated this present community study, which aims to update the previous ESA CCI assessment (Horwath et al., 2022) by introducing two key improvements. First, we extend the sea-level budget assessment to the regional scale, in order to identify the regions where closure breaks down. Second, in addition to the classical approach — where the sum of contributors is compared to the observed total — we test an alternative, inverse method for closing the sea-level budget. In this approach, closure is imposed as a soft constraint, and each contributor is weighted by its corresponding uncertainty, providing an objective framework for imposing closure that explicitly accounts for the relative accuracy of each component. The distance between the posterior and prior estimates of each contributor then serves as a diagnostic metric for assessing the quality of the fit and identifying which contributions require adjustment, and by how much, thereby offering insights into the possible causes of non-closure. Given the central role of uncertainties in the inverse approach, particular attention is paid throughout the paper to the derivation of refined and robust uncertainty estimates.

Section 2 recalls the terminology and methods used to assess the closure of the sea-level budget. Section 3 presents the different estimates of the sea-level budget components with their uncertainties. Section 4 and 5 present the results of the ocean mass and sea-level budget closure assessment. Section 6 discusses the findings.

2 Methodological framework

2.1 Sea-level and global water budgets terminology

The main definitions to refer to sea-level changes and the global water budget used in this manuscript are recalled in this section. The terminology used is mainly defined in Gregory et al. (2019).

https://doi.org/10.5194/essd-2026-627
Preprint. Discussion started: 19 August 2026

At the regional or local scale, the sea-level budget equation is:

$$\Delta R = \Delta R_m + \Delta R_\rho \qquad \text{Eq 35 in (Gregory et al., 2019)} \tag{1}$$

where :

- **Relative sea-level** (ΔR) change is defined as the total water column height change between the sea-surface and the seafloor.

  $$\Delta R = \Delta\eta + \Delta F \qquad \text{Eq 24 in (Gregory et al., 2019)}$$

  where $\Delta\eta$ corresponds to the Absolute sea-level changes measured by satellite altimetry,a.k.a. as geocentric sea-level and ΔF to the seafloor deformation with respect to the ellipsoid. This deformations is due to the deformational, gravitational and rotational effects driven by surface load redistributions. In this study, only the vertical deformation is considered called Vertical Land motion (ΔVLM). The first contribution is the Glacial Isostatic Adjustment coming from millennial time-scales effects (GIA). The second one is associated with the contemporary (decades to centuries) mass redistribution (NGIA). However, in this study all contributions coming from anthropogenic withdrawal of fluids, natural VLM induced by sedimentation transport, volcanism and tectonics are neglected.

  $$\Delta R = \Delta\eta + \Delta F_{GIA} + \Delta F_{NGIA}$$

  .

- **Manometric sea-level** change (ΔR_m) is the component of relative sea-level change attributable to changes in the time-mean local mass of the ocean per unit area, assuming density does not change.

- **Steric sea-level** change (ΔR_ρ) is the component of relative sea-level change attributable to changes in ocean density, assuming that the local mass of the ocean per unit area does not change. It comprises the thermosteric sea-level change, which is due solely to changes in in-situ temperature (ΔR_θ), and the halosteric sea-level change(ΔR_θ), which is due solely to changes in salinity. $\Delta R_\rho = \Delta R_\theta + \Delta R_S$

While at global scale, the sea-level budget equation reads:

$$h = h_B + h_\theta \qquad \text{Eq 43 in (Gregory et al., 2019)} \tag{2}$$

where:

- **Global-mean sea-level** (h or $\Delta GMSL$) represents the change in ocean volume divided by the ocean surface area. Hence GMSL is the global mean of relative sea-level ΔR. Note that the equation 2.1 could be integrated to relate the GMSL with the global-mean absolute sea-level (h_G) through the integration of $\Delta F_{GIA} + \Delta F_{NGIA}$ over the ocean.

- **Barystatic sea-level** change (or h_B or ΔBSL) is the component of global-mean sea-level change (GMSL) due to the addition of water mass to the ocean that previously resided over land (as land water storage or land ice) or in the atmosphere (which contains a comparatively small mass of water). Hence, barystatic sea-level is a good approximation of the global-mean of manometric sea-level.

https://doi.org/10.5194/essd-2026-627
Preprint. Discussion started: 19 August 2026

Open Access Earth System Science Data Discussions

- **Global-mean thermosteric sea-level** ($\Delta GMTSL$ or h_θ) is the global mean of the steric sea-level. Note that only the thermosteric contribution is retained, as the halosteric component is negligible (Gregory et al., 2019, see Appendix 2 in).

Note that due to lack of observations of one or several observing system the term global-mean is used for a restricted spatial mask avoiding, semiclosed seas, high latitudes (over$\pm 66°$), and coastal zones (less than 300 km along continental margins). This mask is used in a consistent way all over the document.

The barystatic sea-level change can be also estimated through the global water mass budget (GWMB), summing up the water mass contributions from the cryosphere (Greenland and Antarctic ice sheets and land glaciers) the liquid water over land and the water vapor content in the atmosphere to the ocean mass change as described in the next equation

$$\begin{aligned} h_B =& \Delta M_{ocean} && /(\rho_{ocean} \cdot surface_{ocean}) \\ h_B =& -(\Delta M_{\mathrm{GIS}} + \Delta M_{\mathrm{AIS}} + \Delta M_{\mathrm{GIC}} + \Delta M_{\mathrm{LWS}} + \Delta M_{\mathrm{WV}}) && /(\rho_{ocean} \cdot surface_{ocean}) \end{aligned} \tag{3}$$

where ΔM_{GIS} and ΔM_{AIS} are the Greenland and Antarctica ice sheet mass loss respectively, ΔM_{GIC} is the glaciers ice mass change, ΔM_{LWS} is the water mass change in the Land Water Storage including land-liquid water and snow, ΔM_{WV} is the total water vapor content in the atmosphere and ρ_{ocean}, $surface_{ocean}$ are the mean density and surface of the ocean.

Closure approaches

Budget closure as sea-level budget, global water budget, energy budgets can be analysed by studying the residuals within the uncertainties (Horwath et al., 2022; Cazenave et al., 2018), by a joint inversion to assess one missing component (Rietbroek et al., 2016) or by an objectively-constrained approach (Stephens et al., 2023). This latter objectively-constrained solution of the sea-level budget is constructed by optimally combining individual sea-level components within their uncertainty bounds, so as to minimise the budget residuals. A weighted least squares approach is used to minimise the sea-level budget residuals. The different components of the sea-level budget are objectively adjusted at each time step using their uncertainty as the least square weight. Budget closure is enforced through a soft constraint within the least squares procedure, as detailed in Appendix A.

In this study, the objective approach will enable us to pinpoint dates and places where the SLB does not close within uncertainties along with the contribution that is most probably responsible for the misclosure. We will compare it to the joint inversion solution at global scale to allow us to evaluate the robustness of each solution and to explain why there is misclosure at some dates and places.

Uncertainty Characterisation

A key aspect of both sea-level budget closure assessment approaches (the classical approach and the alternative one based on the optimal approach) is the robustness of the uncertainty estimates. In previous studies (e.g., WCRP Global Sea Level Budget Group, 2018; Horwath et al., 2022), temporal correlations in errors were not accounted for when estimating uncertainties across various time scales (from interannual to multidecadal). Only trend uncertainties implicitly accounted for temporal error

https://doi.org/10.5194/essd-2026-627
Preprint. Discussion started: 19 August 2026

Open Access Earth System Science Data Discussions

correlation, as they were derived from expert estimates of systematic errors and their impact on trends, drawing on comparisons with independent data or reanalyses, as well as instrumental and geophysical correction cross-validation studies.

In this study, we revisit the uncertainty budget of each individual component on an annual basis, explicitly accounting for temporal error correlations. Trend uncertainties are derived from this uncertainty budget, yielding a consistent set of uncertainty estimates across annual to multidecadal time-scales.

The following section documents the measurement uncertainties of each dataset, defined as the uncertainties associated with the instrumental error and algorithmic approximations of each observing system used to measure an individual sea-level contribution. This refers to the accuracy and precision of each individual subsystem within the SLB observing system, and provides a quantitative measure of how well each component is measured. These uncertainties represent the portion of total uncertainty that can potentially be reduced through improvements in instrumentation and data processing. Other sources of uncertainty such as uncertainty due to the representativeness of the measurand are ignored here and will be the subject of another study.

All uncertainties presented in this work are reported at the 16–84% confidence level (i.e., at the 1σ level, assuming Gaussian distributions for the uncertainties).

The analysis concentrates on two time periods: P1 from January 1993 to December 2022 (the altimetry era) and P2 from January 2004 to December 2022 (the GRACE–Argo era). The start of P1 is guided by the availability of altimetry data. Its end is guided by the availability of the C3S v2021 asbolute sea-level dataset used in this study. Although GRACE was launched in 2002, Argo was not fully deployed until 2 years later. These two factors determine the start of P2 in January 2004. The budgets are assessed for mean rates of change (linear trends) over P1 and P2 at monthly resolution.

Furthermore, as the sea-level budget achieves its optimal closure over the 2005-2015 decade, this interval is selected as our reference baseline. Consequently, for all components throughout the remainder of this study, time series are referenced by subtracting their respective 2005-2015 temporal mean. Likewise, component uncertainty envelopes are centered on this baseline window, as it corresponds to the period in which we have the highest confidence in the performance of each individual observing system.

3 Datasets

3.1 Glacial isostatic adjustment and sea-level fingerprints

The Glacio-Isostatic Adjustment (GIA) represents the global response of the solid-Earth to the spatial redistribution of mass upon its surface associated with the melting of cryospheric loads. GIA processes induce vertical and horizontal deformations of the Earth surface, perturbations of the gravitational field, and changes in the geoid that affects absolute sea-level. In this work, we have considered separately two distinct contributions: the still ongoing effects due to the melting of late-Pleistocene ice-sheets (GIA) and the response to the climate-driven, contemporary ice-sheet mass loss (NGIA). The first contribution is a consequence of the isostatic disequilibrium still present after the progressive disintegration of the ice sheets after the Last

https://doi.org/10.5194/essd-2026-627
Preprint. Discussion started: 19 August 2026

Glacial Maximum and is accounted for by invoking a viscoelastic rheology for the mantle. The latter can instead be explained, on the timescales of a few decades considered in the present work, in terms of the purely elastic response of the Earth to the mass exchange between land-based cryosphere and the ocean.

3.1.1 Methods and product

In this study, GIA in response to the late-Pleistocene deglaciation has been simulated by solving the Sea-Level Equation (SLE), which describes the GRD effects caused by the waxing and waning ice-sheets, originally introduced by Farrell and Clark (1976). This has been accomplished by using the standard version of the pseudo-spectral gravitationally and topographically self-consistent SELEN^4 code (Spada and Melini, 2019). The SLE solution has been obtained on a geodesic grid (Tegmark, 1996) with a global spatial resolution of ~ 40 km, expanding all scalar fields to maximum harmonic degree $l_{max} = 512$ and adopting the iterative process described in Spada and Melini (2025). SELEN^4 assumes a spherically symmetric Earth with an elastic lithosphere, a linear Maxwell incompressible rheology and an inviscid homogeneous core.

The contribution of NGIA to the present-day sea-level fingerprints and to the rates of change of the Stokes coefficients of the gravitational field are given according to a realization, within SELEN^4, of the ICE-6G (VM5a) model of Argus et al. (2014) and Peltier et al. (2015). In SELEN^4, the rotational feedback on sea level has been implemented by means of the "revised rotational theory" of Mitrovica et al. (2005), as discussed in Spada and Melini (2025).

Depending on the use, GIA and NGIA fingerprints may be expressed as: (a) present-day rate of geoid height variation in the reference frame of the rotating Earth ($\dot{G}$), (b) the rate of absolute sea-level change as seen by satellite altimetry ($\dot{N}$), (c) the rate of geoid height variation in the inertial non-rotating frame ($\dot{G}_{Grace}$), as seen by GRACE (Tamisiea, 2011), where the overdot denotes the (constant) rate of change of the corresponding GIA variables (see figure 1) These fingerprints are not independent of each other, since $\dot{N} = \dot{G} + \dot{c}$ where $\dot{c} \approx -0.2\ mm\ yr^{-1}$ and $c(t)$ is a spatially invariant term that ensures mass conservation within the Earth system (Farrell and Clark, 1976). At the same time, the SLE reads $\dot{N} = \dot{S} + \dot{U}$ where S is the change in sea-level relative to the solid Earth and U is the vertical displacement of the Earth's surface (Spada and Melini, 2025). By considering the quantities introduced in Section 2.1, the contributions to S, N and U due to GIA are relevant for ΔR, $\Delta\eta$ and ΔF, respectively. Furthermore, while the global ocean average of the GIA induced relative sea-level rate ($\dot{S}$) strictly integrates to zero over the full global ocean ($\pm 90°$), restricting the spatial integration to the mask used in this study introduces a negligible difference of only 0.01 mm yr^{-1}, which is statistically non-significant compared to the GIA model uncertainties. As discussed by Tamisiea (2011), fingerprints of $\dot{G}$ and $\dot{G}_{Grace}$ differ only by the long-wavelength Stokes coefficients $\dot{c}_{21}$ and $\dot{s}_{21}$, associated with variations in the centrifugal potential due to the GIA-induced drift of the Earth's pole of rotation. The long-wavelength four-lobe pattern in all fingerprints of Figure 1 manifests the importance of Earth rotational variations (polar motion) in GIA.

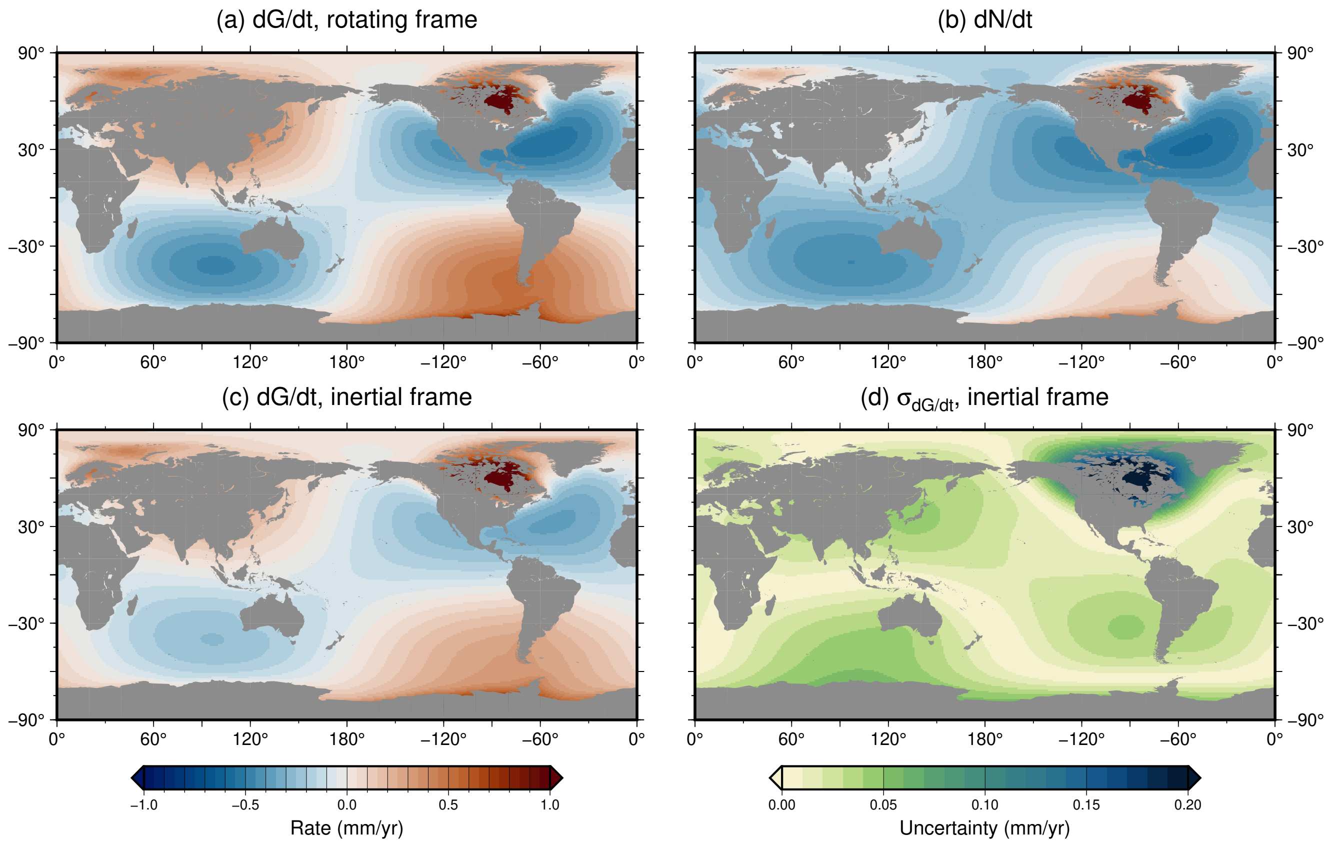

Figure 1. Present-day rates of change of geoid height (a) and sea surface height (b) due to the ongoing effects of GIA according to the SELEN^4 realization of the ICE-6G(VM5a) model by Argus et al. (2014) and Peltier et al. (2015), evaluated in a rotating reference frame. For the same GIA model, the rate of change of geoid height in a non-rotating frame and its associated model uncertainty (1-σ) are shown in frames (c) and (d), respectively.

Sea-level fingerprints due to the variation in mass of present day ice sheets, glaciers and LWS have been obtained by solving a purely elastic variant of the gravitationally self-consistent SLE. This has been accomplished by means of a suitably modified version of the SELEN^4 code, in which the solution is obtained entirely in the spatial domain to avoid aliasing effects arising from the spectral representation of small-scale surface load elements. The elastic response has been modeled assuming a fully compressible Earth model with a spherically symmetric density and elastic constant variation, adopting the seismological reference model “REF” of Kustowski et al. (2008). The rates of geoid change over the time window 2002-2020 in response to the mass variation are computed for different regions: Antarctic ice sheet, Greenland ice sheet, glaciers and the cumulative response including the three components of the ice mass and variations in the LWS. (See NGIA average rates of geoid change in Appendix B).

https://doi.org/10.5194/essd-2026-627
Preprint. Discussion started: 19 August 2026

3.1.2 Uncertainty assessment

Structural model uncertainties associated to GIA have been evaluated as standard deviations over a mini-ensemble of 20 variations of the VM5a rheological profile already considered by Roy and Peltier (2015). These variants of the rheological profile are all consistent with observed paleo-shorelines and include different assumptions about the thickness of the lithosphere, viscosity of the upper mantle, transition zone and lower mantle, and viscosity contrast between upper and lower mantle. For each variant of the VM5a profile, predictions of the rate of change for geoid in the inertial non-rotating frame ($\dot{G}_{Grace}$) have been obtained by solving the SLE, and the corresponding standard deviation has been evaluated with respect to $\dot{G}_{Grace}$ from the nominal (*i.e.*, unperturbed) VM5a profile. The uncertainty of the $\dot{G}_{Grace}$ GIA fingerprint reaches its maximum amplitude of $\sim 0.2\ mm\ yr^{-1}$ in the Hudson bay (see Figure 1d). The modeling uncertainty on fingerprints has been estimated by using different sets of loading Love numbers, pertaining to different Earth's elastic structures globally consistent with seismological observations. The relative uncertainty on the fingerprints does not exceed 5%.

3.2 Absolute sea-level and GMSL

3.2.1 Methods and product

Satellite radar altimetry observes sea-surface height variations measured with respect to a reference ellipsoid centred on the Earth's center of mass. This sea-surface height corresponds to absolute sea-level ($\Delta\eta$). We use the daily gridded absolute mean sea-level anomaly distributed by the Copernicus Climate Change Service (C3S) Climate Data Store (Copernicus Climate Change Service, 2018). In this study the version vDT2021 of the dataset is used. This dataset is providing global gridded $0.25° \times 0.25°$ dataset over the $82°N - 82°S$ latitude range. The time coverage is starting from January 1993 and ending in September 2023. To ensure long term stability, two missions are used simultaneously at each time as a baseline reference: the current reference mission (TOPEX/Poseidon, Jason-1, Jason-2, Jason-3 and Sentinel-6 Michael Freilich) and an auxiliary mission from the altimetry constellation.

Long-term instrumental drifts are corrected following the C3S recommendations. In particular, the TOPEX-A altimeter drift correction (Dieng et al., 2017) provided in the C3S dataset is applied. For the drift affecting the Jason-3 Wet Troposphere Correction (WTC), a correction is performed using the dataset of Brown et al. (2023). Since this correction is available along-track, we estimated its corresponding global mean time series through the standard AVISO procedure to directly correct the global mean absolute sea-level time series. At the local scale, the gridded fields are adjusted at each time step by applying a spatially constant value deduced directly from this global correction time series.

Daily absolute mean sea surface fields are aggregated to monthly means and spatially averaged from the native $0.25° \times 0.25°$ grid onto a $1.00° \times 1.00°$ grid using ocean-area-weighted means.

https://doi.org/10.5194/essd-2026-627
Preprint. Discussion started: 19 August 2026

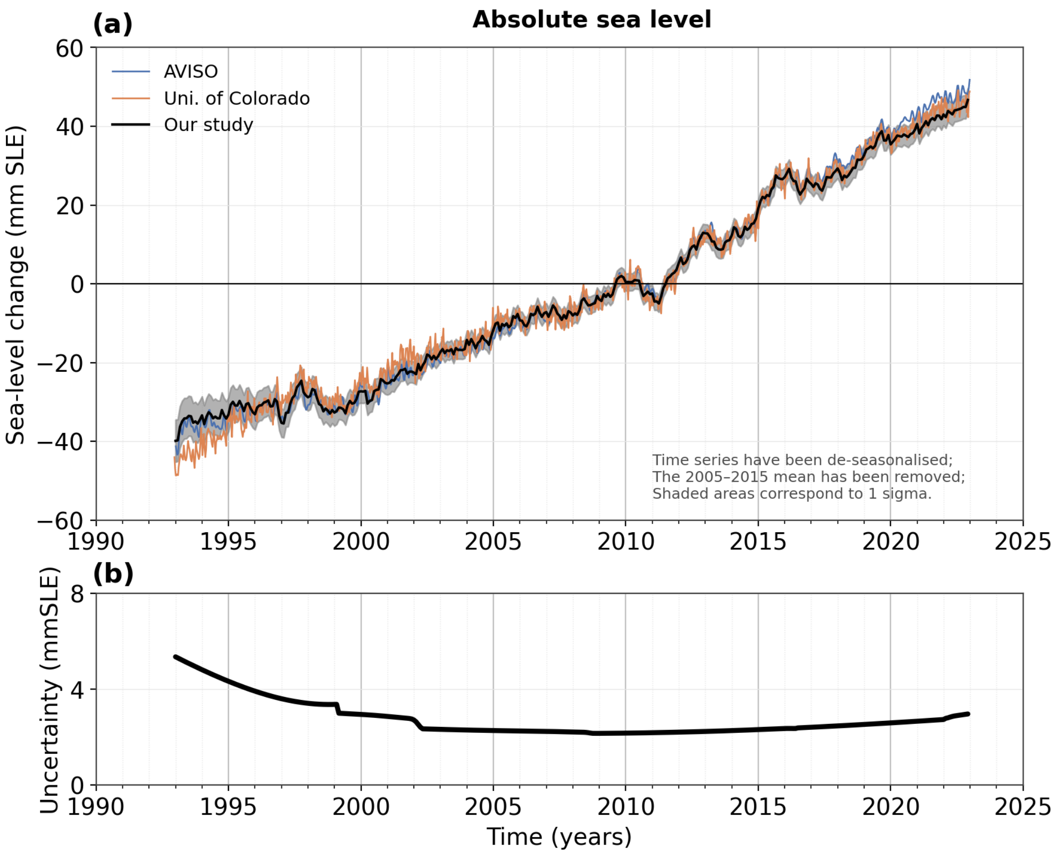

Figure 2. Global mean absolute sea-level: (a) comparison of AVISO (blue line), University of Colorado (orange line) and this study (black line) global mean relative sea-level estimations with $1-\sigma$ uncertainty envelop; (b) Uncertainties assessed for the estimates in (a)

Global mean absolute sea level is also computed by AVISO product (https://www.aviso.altimetry.fr/) and University of Colorado (Nerem et al., 2010; University of Colorado Sea Level Research Group, 2026). While all estimates exhibit excellent overall agreement across the whole time series, localized small discrepancies emerge during the TOPEX era (see figure 2a) Nevertheless, the resulting linear trends over the 1993-2022 period remain remarkably close, yielding values of 2.95 $mm\ yr^{-1}$ for the University of Colorado, 3.01 $mm\ yr^{-1}$ for AVISO, and 2.85 $mm\ yr^{-1}$ for our study. These trend differences remain not statistically significant when evaluated against our prescribed trend uncertainty of $\pm 0.18\ mm\ yr^{-1}$ over this same timeframe (detailed in the following section).

Relative sea-level is computed following Eq: 2.1 by adding GIA and NGIA effects to the absolute sea-level. More details on these corrections have been provided in section 3.1. For the remainder of this study, our analysis focuses specifically on relative sea level (ΔR) and the corresponding global-mean sea-level (GMSL).

https://doi.org/10.5194/essd-2026-627
Preprint. Discussion started: 19 August 2026

3.2.2 Uncertainty assessment

Uncertainties in the altimetry-based GMSL are estimated following the methodology of Ablain et al. (2019), with updates from Guérou et al. (2023) and Cadier et al. (2024), the latter specifically updating the uncertainty budget for the Sentinel-6 Michael Freilich mission. Furthermore, the uncertainty budget presented here also benefits from improvements developed within the ESA ASELSU project. The main sources of uncertainty include instrumental noise, orbit determination, geophysical corrections, and residual inter-mission biases. Here, unlike Guérou et al. (2023), the uncertainty associated with the radiometer WTC is not considered over the Jason-3 period, since the Jason-3 WTC drift is corrected using the correction provided by Brown et al. (2023).

The specific error parameters of the sea-level Rise Stability Uncertainty Budget (see Table 1) are derived from continuous calibration and validation (Cal/Val) activities of successive reference altimetry missions. Each contributor to the global-mean sea-level error budget is characterized by its physical origin and its mathematical covariance structure over time. These error sources are systematically categorized into four main components: short-term time-correlated effects (with typical timescales of 1 to 6 months), long-term time-correlated stability shifts (such as a 5-year correlation for the WTC or a 10-year scale for precise orbit determination errors), linear time-correlated trends (such as uncertainties arising from GIA modeling and ITRF realization limits), and uncertainties related to inter-mission offsets calculated during tandem flight phases.

By defining explicit standard deviations, drift rates, or bias thresholds for each individual contributor, the variance-covariance matrix of the global mean sea-level can be obtained following Ablain et al. (2019). This enables a consistent propagation of altimeter uncertainties to long-term climate trend and acceleration metrics, with the resulting uncertainty envelope displayed in Figure 2b.

https://doi.org/10.5194/essd-2026-627
Preprint. Discussion started: 19 August 2026

Open Access Earth System Science Data Discussions

Table 1. Sources of uncertainties of the global mean sea-level and their estimates and their corresponding standard deviation estimation (Ablain et al., 2019; Guérou et al., 2023; Cadier et al., 2024)

Source of uncertainties	Temporal structure of error	Standard uncertainty u at 1-sigma
Random noise due to altimeter measurements and altimeter-dependant corrections, precise orbit determination, atmospheric and environmental corrections, mean sea surface, oceanic variability	Short-term time-correlated effects at 1 month	$u = 1.7$ mm (TP) $u = 1.2$ mm (J1) $u = 1.1$ mm (J2) $u = 1.0$ mm (J3) $u = 1.1$ mm (S6MF)
	Short-term time-correlated effects at 6 months	$u = 1.4$ mm (TP) $u = 1.2$ mm (J1) $u = 1.1$ mm (J2) $u = 1.1$ mm (J3) $u = 1.3$ mm (S6MF)
Wet troposphere correction stability	Long-term time-correlated effects at 5 years	$u = 1.1$ mm
Orbit determination	long-term time-correlated effects at 10 years	$u = 1.1$ mm (TP) $u = 0.5$ mm (J1/J2/J3)
Inter-missions global-mean sea-level offset	Anti-time-correlated effects from each part of the offset	$u = 2.0$ mm (TPA/TPB) $u = 0.6$ mm (TP/J1) $u = 0.2$ mm (J1/J2) $u = 0.4$ mm (J2/J3) $u = 0.5$ mm (J3/S6MF)
ITRF	Linear time-correlated effects	$u = 0.1$ mm yr^{-1}
GIA	Linear time-correlated effect (drift)	$u = 0.05$ mm yr^{-1}
Altimeter parameters stability	Linear time-correlated effects	$u = 0.7$ mm yr^{-1} (TPA) $u = 0.1$ mm yr^{-1} (TPB)

This framework has also been performed in Prandi et al. (2020) to characterize uncertainties in the regional sea-level anomaly. At the $2° \times 2°$ regional scale and yearly time scale, the altimetry error budget is derived by assessing the same key components (instrumental noise, WTC, orbit determination, and geophysical corrections) while explicitly modeling their regional variability, such as geographically dependent orbit errors or localized radiometer stability shifts. These errors are characterized according to their temporal behavior (short-term anomalies, long-term stability variations, and linear drifts). By combining the standard deviations and correlation timescales, a regional temporal variance-covariance matrix is constructed

https://doi.org/10.5194/essd-2026-627
Preprint. Discussion started: 19 August 2026

305 for every grid point to enable regional trend and acceleration uncertainty estimation (see Table 2).

Table 2. Sources of uncertainties of the local sea-level change and their estimates, update from Prandi et al. (2021). Location-dependent uncertainties are provided in the Prandi et al. (2020) dataset.

Source of uncertainty	**Temporal structure of error**	**Standard uncertainty u at 1-sigma**
Short time-correlated errors due to POD, altimeter parameter, geophysical corrections	Short-term time-correlated effects at 1 year	6 mm < u < 9 mm (vary spatially) (Prandi et al., 2020)
Wet tropospheric correction stability	Long-term time-correlated effects at 10 years	1 mm < u < 3 mm (vary spatially) (Prandi et al., 2020)
Precise orbit determination stability	Linear time-correlated effect	$u = 0.33$ mm yr^{-1}
GIA correction	Linear time-correlated effect	u < 0.3 mm yr-1 (vary spatially) (Prandi et al., 2020)
Mean sea-level offset estimate	Anti-time-correlated effects from each part of the offset	$u = 10$ mm (TPA/TPB) $u = 2$ mm (TPB/J1, J1/J2, J2/J3, J3/S6)

3.3 Steric sea-level and GMTSL

To determine sea-level changes due to steric effects, datasets and methodologies differ depending on the scale considered. We use interpolated in situ temperature and salinity products for the global-mean thermosteric sea-level, the regional thermosteric
310 sea-level, and the regional halosteric sea-level. We build on OI-products intercomparison studies (Bagnell and DeVries, 2023; Hakuba et al., 2024), to assess the skill of various observational-based analyses to represent fluxes of heat and freshwater, which constitute good criteria for determining suitable estimates of thermosteric and halosteric sea-level changes.

3.3.1 Methods and product

The estimates of GMTSL from EN4 (version 4.2.2, Good et al. (2013)) gridded product spans the altimetry era (i.e., from 1993
315 to 2024). EN4 product is based on an optimal interpolation of the quality-controlled in situ temperature measurements over the 20th and 21st centuries. The EN4 product also provides an uncertainty estimate at each grid point. We use this estimate to derive the local steric sea-level uncertainty and to derive the GMTSL uncertainty estimate.

At regional scale, SIO (version 2020, Roemmich and Gilson, 2009) and JAMSTEC (version 2023, Hosoda et al., 2008), ISAS20 (Gaillard et al., 2016; Kolodziejczyk et al., 2023), ISHII (Ishii et al., 2003, 2006) and IAP (Cheng and Zhu, 2016)
320 products are considered to estimate regional steric sea-level changes down to 2000 m depth, and associated uncertainties. SIO, JAMSTEC, IAP and ISAS are notably compared to the GMTSL derived from EN4, over the altimetry era or Argo period when available, in order to validate it (Fig. 3a).

https://doi.org/10.5194/essd-2026-627
Preprint. Discussion started: 19 August 2026

The SIO product was primarily selected to estimate the regional halosteric and thermosteric contributions, from 2002 to 2024 as it does not experience spurious behavior after 2015/2016 (Barnoud et al., 2021; Ponte et al., 2021; Liu et al., 2024). The evolution of the global salinity (estimated by interpolating in situ observations with autoregressive artificial neural networks) has been compared to these obtained from several gridded products (ISAS20, JAMSTEC, SIO), and SIO displays also the closest trend in the global freshening (Bagnell and DeVries, 2023). Indeed, SIO analysis applies a strict control on the quality of the Argo data used, notably through bias evaluation and correction especially on near real time salinity profiles (Wong et al., 2023).

JAMSTEC is selected also for the thermosteric contribution because its associated global ocean heat content signal correlates higher than with other similar products (SIO, EN4...) with the estimated ocean heat uptake from CERES (Hakuba et al., 2024). ISHII and ISAS20 are not covering the whole target period, and IAP uses model outputs in their analysis which could introduce errors due to the model biases.

Nevertheless, ISAS20 grid and vertical levels were used to re-interpolate EN4, and make it compatible with the codes and covariance matrices already designed for calculating the steric sea-level changes and uncertainties with ISAS20. Additionally, ISAS20 and ISHII are used to calculate the uncertainty in the regional thermosteric and halosteric estimates (discussed below).

Table 3 summarizes the different OI products used for the steric sea-level contributions. SIO and ISAS20 are based on Argo data only, while the others use various kinds of in situ observations. These products use climatologies originating from the World Ocean Atlas (EN4, JAMSTEC, ISAS20, ISHII), from their own interpolation procedure (SIO), or using CMIP5 model data (IAP). Signals from observations are propagated spatially and temporally, given scales of decorrelation that vary with latitude or depth.

https://doi.org/10.5194/essd-2026-627
Preprint. Discussion started: 19 August 2026

Table 3. Summary of the implementation and parameters used in EN4, JAMSTEC, SIO, ISAS20, IAP, and ISHII products.

Name and reference	Interpolated data	First guess	Correlation scales
EN4 (Good et al., 2013) Version 4.2.2	All types of data. L09 (Levitus et al., 2009) corrections.	Monthly (1971-2000) climatology added to a persistence based forecast	300 and 400 km (increased near equator) horizontal scales. 100 and 200 m vertical scales.
JAMSTEC (Hosoda et al., 2008) version 2023	Argo floats, TRITON buoys, CTD casts	Monthly (Seasonal below 1500dbar) mean WOA01 climatology	Depth dependent zonal and meridional decorrelation radii ranging from 3° to 24° horizontally
SIO (Roemmich and Gilson, 2009) Version 2020	QC Argo data only	Monthly field obtained by a locally weighted least square fit	140 and 1111 km, with an increase near the equator
ISAS (Kolodziejczyk et al., 2023) 2020	QC Argo data only	Monthly World Ocean Atlas 2018 (A5B7 version)	300km and 6 × the 1st Rossby Radius of deformation
IAP (Cheng and Zhu, 2016) V3	All types of data. C14 (Cheng et al., 2014) corrections	Ensemble averages of CMIP5 historical simulations (before 2005) and RCP4.5 simulation outputs (after 2006)	Iterative analyses with 20° (25° below 700 m), 8° and 4° influence radii
ISHII (Ishii et al., 2003, 2006) V6.4	All types of data.	Monthly World Ocean Atlas 2001	Depth dependent decorrelation scales, starting at 300km horizontally, 10 m vertically, and 15 days temporally, and increasing with depth (Ishii et al., 2006).

Below 2000-m depth, more uncertainty lies due mainly to the lack of observations. However, an estimate of the contribution of the deep sea thermal expansion ($0.1 \pm 0.1\ mm\ yr^{-1}$) was considered, based on the work of Purkey and Johnson (2010).

The thermosteric component of SLC is estimated such as:

345 $$\int_{z=0}^{2000m} -\frac{\delta\rho[T(\boldsymbol{x},t),S_0]}{\rho_0}dz, \tag{4}$$

https://doi.org/10.5194/essd-2026-627
Preprint. Discussion started: 19 August 2026

with z the depth, $\delta\rho[T(\boldsymbol{x},t),S(\boldsymbol{x},t)] = \rho[T(\boldsymbol{x},t),S(\boldsymbol{x},t)] - \rho[T_0 = 0, S_0 = 35.16504]$, ρ the density, depending on T the temperature and S the salinity, $\boldsymbol{x}$ the three-dimensional position vector, t the time, and $\rho_0 = 1026\ kg\ m^{-3}$. The halosteric component is estimated similarly, but with varying salinity and constant temperature $T_0 = 0\ °C$. The steric sea-level is the sum of thermo- and halosteric components.

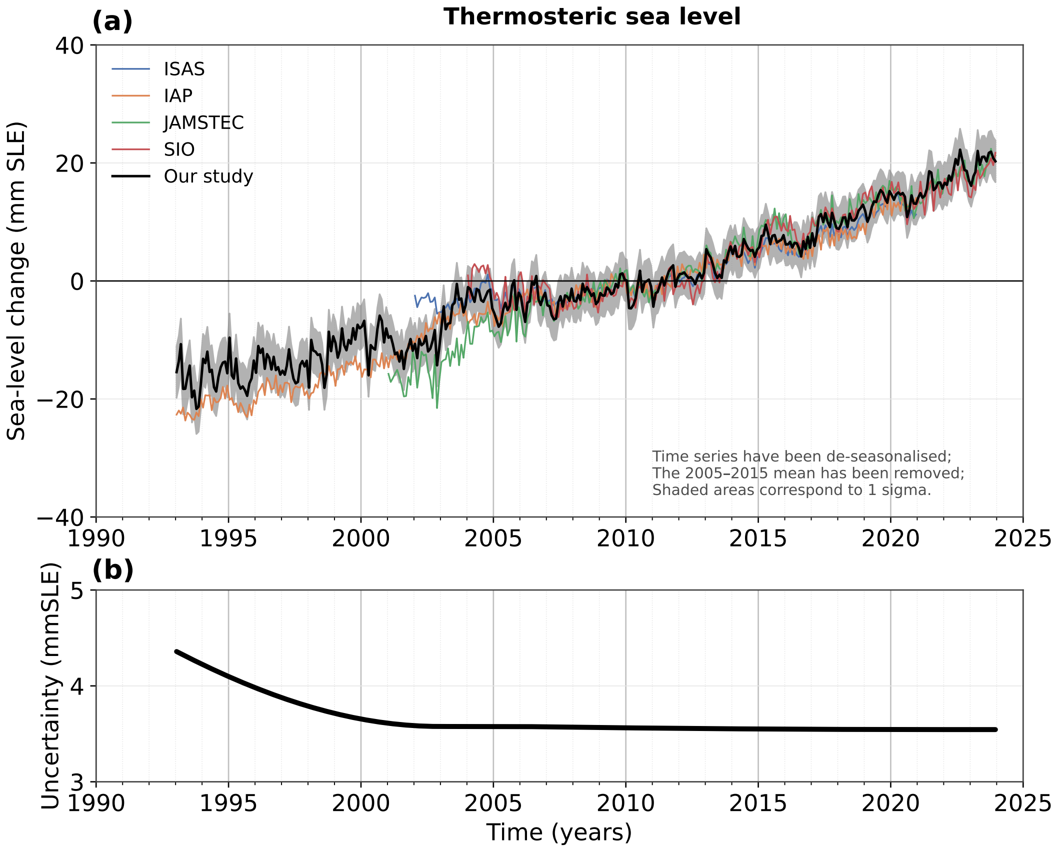

Figure 3. Global mean thermosteric sea-level: (a) comparison of ISAS (blue), IAP (orange), JAMSTEC (green) and SIO (red). Product used in this study is in black with $1-\sigma$ uncertainty envelop; (b) Uncertainties assessed for the estimates in (a)

3.3.2 Uncertainty assessment

Computing the error in GMTSL requires to assess the error in density (σ_ρ). The error on each density estimate is propagated from analysis error provided along with temperature and salinity estimates in the EN4 fields (e.g., Good et al., 2013). To allow considering the non-linearity in the density calculation from temperature, while simplifying the calculation, the thermal expansion coefficient is approximated as $\alpha(\boldsymbol{x},t) \approx 0.07 + 0.0137\ T(\boldsymbol{x},t)$ (Roquet et al. (2015)). The error of the density is thus:

$$\sigma_\rho(\boldsymbol{x},t) = \alpha(\boldsymbol{x},t,T(\boldsymbol{x},t))\ \sigma_T^a, \qquad (5)$$

https://doi.org/10.5194/essd-2026-627
Preprint. Discussion started: 19 August 2026

where σ_T^a is the error of the temperature estimate.

Then, when calculating the error $\sigma_{TSL}(\boldsymbol{x}_{horizontal}, t)$ on the vertically integrated TSL, one can consider the correlation among the depth levels to estimates in the summation of the individual error at each level. It follows :

$$\sigma^2_{TSL}(\boldsymbol{x}_{horizontal}, t) = \sum_z [\frac{\Delta Z(z)\sigma_\rho(\boldsymbol{x}, t)}{\rho_0}]^2 + \sum_z \sum_{z_2 \neq z} \xi(\boldsymbol{x}(z), \boldsymbol{x}(z_2))[\frac{\Delta Z(z)\sigma_\rho(\boldsymbol{x}(z), t)}{\rho_0}][\frac{\Delta Z(z_2)\sigma_\rho(\boldsymbol{x}(z_2), t)}{\rho_0}], \quad (6)$$

where $Z(z)$ is the layer thickness at depth z, and $\xi(z, z_2)$ is the vertical covariance between two depth levels z and z_2. This vertical covariance sets the correlation between the vertical levels, i.e., the effective degree of freedom of the temperature variability over the vertical. It is used to accurately calculate the error on the integrated thermosteric estimate at each grid point of the analysis. This vertical correlation matrix is illustrated in Supplementary Figure C1, with the example of a water column located along the equator, in the tropical Pacific (180°E-1°S).

The vertical covariance in Eq. (6) is estimated for each box of 3°×3° using the time series of temperature provided by ISAS20 analyses. The temperature uncertainty from EN4 is used to calculate the global thermosteric sea-level change error.

Eventually, to obtain the uncertainty in the GMTSL change (horizontal average), its average is calculated, with the effective number of degrees of freedom N^* determined following von Schuckmann et al. (2009). In their approach, they find that a spatial correlation scale of 300 km divides the degree of freedom N in a global average such as: $N^* \sim N/177$. The uncertainty in the GMTSL is shown in figure 3b.

A limitation of EN4 is the absence of uncertainty estimates below 1000 m (due to insufficient observational sampling, preventing the application of the method previously described) and over 10 m. To remedy this issue, the errors at 1000m were simply extended downwards and at 10m upward. This uncertainty is then used to calculate the GMTSL error.

To calculate the uncertainties of the regional thermosteric and halosteric estimates, a different approach from the GMSTSL is used. A spread estimate of an ensemble including EN4, ISAS20, JAMSTEC, SIO and ISHII is used to quantify the uncertainties around the singular thermosteric (JAMSTEC) and halosteric (SIO) estimates.

3.4 Manometric sea-level and Barystatic sea-level

The GRACE (2002-2017, Tapley et al. (2004)) and GRACE-FO (launched 2018, Landerer et al. (2020)) satellite gravimetry missions have observed temporal changes of Earth's gravitational field. Once the gravitational effects of solid-Earth processes are removed, the remaining temporal gravity field variations can be used to infer temporal variations of the surface mass distribution. We use the TU Dresden Level-3 (L3) global gridded product on surface mass changes (in units of $kg\ m^{-2}$) developed for this study (ATBD, 2025). It is based on GRACE Level-2 (L2) monthly gravity solutions provided in a spherical harmonic (SH) representation. This gives us full access to, and control of, methodological choices and uncertainty characterisation. The method is summarized in the following.

3.4.1 Methods and product

The TU Dresden L3 gridded product methodology is a further development of the framework elaborated by Döhne et al. (2023). The method can be described as a L2-based mascon (mass concentration) method, similar to Croteau et al. (2021). It incorporates error variances and covariances of the input L2 solutions and signal variances and covariances of the expected mass redistribution signals. The method can also be described as a method of tailored sensitivity kernels (Döhne et al., 2023). Indeed, Döhne et al. (2023) showed that the two perspectives are equivalent as long as they rigorously employ the same variance-covariance information on both the mass redistribution signal and the L2 solution errors.

The input L2 solutions are the ITSG2018 series of GRACE and GRACE-FO SH solutions (Kvas et al., 2019) expanded up to SH degree and order 96. Previous assessments have indicated that ITSG2018, together with, and slightly superior to, CSR RL06 have the lowest noise level and the best signal retaining among the assessed L2 solutions (Ditmar, 2022; Meyer et al., 2024). Moreover, the ITSG2018 solutions's publication includes error covariance matrices.

The gravitational effect of GIA is subtracted from the L2 solutions, employing the GIA model output described in Sect. 3.1. Degree-1 coefficients are calculated in a way similar to Technical Note 13 (TN-13) by the GRACE/GRACE-FO Science Data System (Sun et al., 2016; Swenson et al., 2008) but utilizing the ITSG2018 L2 solutions and the GIA model used in this study (cf. Sect. 3.1) to ensure the consistency. C_{20} coefficients, as well as C_{30} coefficients for the time after 2016-09, are replaced by estimates from satellite laser ranging provided in TN-14 (Loomis et al., 2025). The AOD (atmospheric and oceanic de-aliasing model) applied during GRACE L2 product generation is restored in the way recommended by Uebbing et al. (2019).

Mascons are defined at an equal-area (approximately 120 km x 120km) grid, where each grid cell is assigned to either the ocean, the ice sheet, or the land domain (other than ice sheet). Each mascon is amended by a global pattern of ocean mass change representing its gravitationally consistent sea-level fingerprint. In this way, the applied constraints on oceanic mascons do not affect ocean mass redistribution related to 'passive' sea-level fingerprints but only any additional, ocean dynamic mass redistribution. For consistency with other gridded datasets in this study, the L3 solutions are ultimately interpolated to 1°x 1° equal-angle grids, ensuring mass conservation within each domain.

As for the L2 solution error variance-covariance information, the formal error covariance matrix of the ITSG2018 solutions are used, adopting their temporal mean over 2003-01 – 2016-08 for the entire time series. As for the signal variance, an iterative procedure similar to Croteau et al. (2021) is used, driven by the variance of the preliminary mass change time series. Starting with a 275 km Gaussian filtered gridded time series, signal variances for land and ice-sheet mascons are determined iteratively. Signal variances for ocean mascons are set to the median of all ocean mascon variances in each iteration step. Spatial covariances (according to a Gaussian autocorrelation with 300 km one-sigma correlation lengths) are prescribed between mascons within the same domain (land, ice-sheet, or ocean).

The barystatic sea-level computed with this product is compared with the state-of-the-art (See Figure 4). Every product has been computed using the consistent ocean mask used in this study (see 2.1). Notably, evaluating the impact of latitude coverage reveals that the trend difference between using a $\pm 90°$ and a $\pm 66°$ mask is 0.15 mm yr^{-1}, which is non-significant compared to the trend uncertainty (0.28 mm yr^{-1}). With the exception of SLBC-1 product used by Horwath et al. (2022), these time

https://doi.org/10.5194/essd-2026-627
Preprint. Discussion started: 19 August 2026

series overlap largely within the one-sigma error confirming the maturite of the products. Horwath et al. (2022) used a different GIA model (Caron et al., 2018), which implied a larger GIA correction effect and hence larger barystatic sea-level rates.

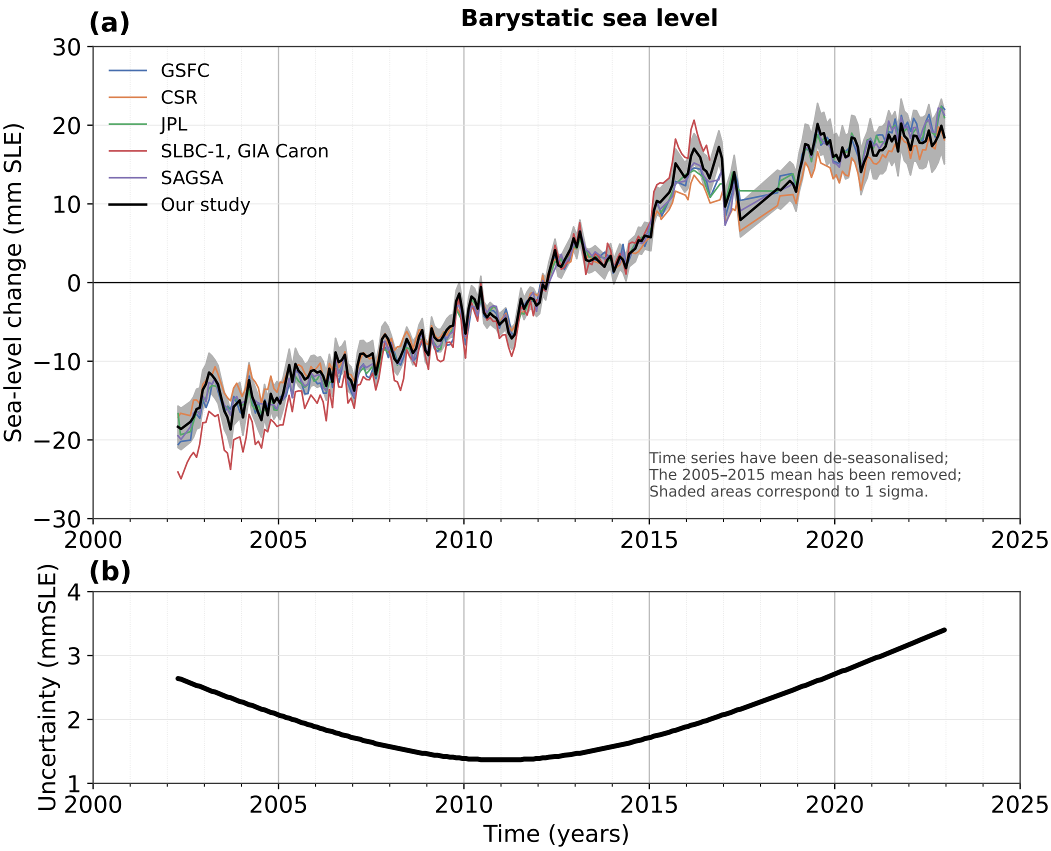

Figure 4. Global barystatic sea-level time series changes. (a) time series from the following satellite-gravity based solutions: our study (black curve), GSFC RL06v2.0 Mascons (Loomis et al., 2019) (blue curve), CSR RL06.3 Mascons (Save et al., 2016) (orange curve), JPL RL06.3 Mascons (Wiese et al., 2016) (green curve), our previous study (Horwath et al., 2022) (red curve) and SAGSA V2.2 (Blazquez et al., 2018) (b) uncertainty assessed for the time series of our study

3.4.2 Uncertainty assessment

The error variances and temporal covariances of the time series of regionally integrated mass changes, such as the global ocean mass change are constructed from separate assessments of errors from the following sources: (a) uncorrelated noise propagated from the GRACE L2 solutions; (b) errors propagated from the low-degree harmonics (degree-one, C_{20}, C_{30}); (c) leakage errors; and (d) uncertainties in modelled geophysical corrections, most importantly for GIA. The methods to assess the individual error sources and to construct the related error covariance matrices are a refinement of the methods used by Groh and Horwath (2021) and are described in further detail by UCR (2025).

(a) Following Groh and Horwath (2021) the uncorrelated-noise component of the time series is assessed by the RMS of a high-pass filtered time series, scaled with a factor that compensates for the attenuation of the RMS of white noise by the high-pass filtering.

(b) Following Groh and Horwath (2021) ensembles of alternative low-degree harmonics time series are used and the spread of the ensembles is taken as an indication of their uncertainty. Particularly, we use the spread of linear trends of the ensemble members to assess the uncertainty propagated to the linear trend of the mass change time series.

(c) We assess leakage errors by simulations, similarly to Groh and Horwath (2021), but with an updated and extended set of synthetic models. The simulations use synthetic signals of land water storage changes, glacier mass changes, ice-sheet mass changes, and ocean dynamics changes. The synthetic signals are converted to their gravity field effect in the SH domain. They are then processed in the same way as the GRACE L2 solutions are processed. The difference between the resulting simulated mass change solutions and the original synthetic mass change models represent the simulated leakage effects. We assess the temporally linear component of leakage from the linear components of the simulated leakage errors.

(d) Following Horwath et al. (2022) the uncertainty of the GIA correction is assessed from the spread among an ensemble of several GIA corrections detailed in Horwath et al. (2022) .

Error covariance matrices of each individual error source are summed up to the full error covariance matrix of the mass change time series.

3.5 Glacier mass change

This component comprises all land ice other than the ice sheets covering Greenland and Antarctica including what are termed the peripherical glaciers and ice caps (PGIC) around the margins of the ice sheets. GIC are typically divided into 19 regions that are considered loosely climatically homogeneous (RGI 7.0 Consortium, 2023). Regions 5 and 19 represent PGIC in Greenland and Antarctica, respectively and require special treatment as discussed below.

There are over 200,000 GIC worldwide with only a few hundred possessing multi-annual in-situ estimates of mass balance, while the vast majority of satellite mass balance observations that provide global coverage, cannot resolve individual glaciers (see Supplementary Figure D1). A notable exception to this is a global DEM differencing data set derived primarily from ASTER imagery (Hugonnet et al., 2021). This data set has, however, limited temporal resolution and is typically used to provide a 20-year mean mass balance rate at glacier resolution for the period post 2000. A novel solution to this quandary, has been developed by combining the high temporal resolution in-situ data with the high spatial resolution satellite observations by geostatistical modelling making the assumption that inter-annual variability has some spatial coherence (Dussaillant et al., 2024).

3.5.1 Methods and product

Here we use the 0.5 degree gridded data set as this provides adequate resolution for calculating the sea-level fingerprint due to GRD effects. For this purpose, however, it is beneficial that the time series includes a seasonal cycle rather than the annual mean, which was the temporal resolution of the original glacier mass balance product. Here, we add an idealised seasonal cycle based on a sine wave function following the approach of Zemp et al. (2025) with an amplitude determined at the glacier region level given by the summer and winter balances as determined from in-situ observations that resolve these at the hemispheric level. The exception to this, is region 16, tropical glaciers, where no seasonal cycle is apparent and therefore monthly mass balances are distributed through the calendar year. Special care is required for PGIC as, for some methods such as satellite gravimetry, it is difficult to separate the signal from PGIC and the adjacent ice sheet. Other methods, such as satellite altimetry volume change estimates should, in principle, be able to partition between the two components. The ice sheet mass trends used in this study attempt to exclude PGIC, which means that they are part of the GIC component. Figure 5a shows the cumulative GIC trends for the period of relevance here, although the full time series extends back to 1978. For comparison, we also show the trend excluding PGIC to show the magnitude of this component compared to GIC outside of Greenland and Antarctica.

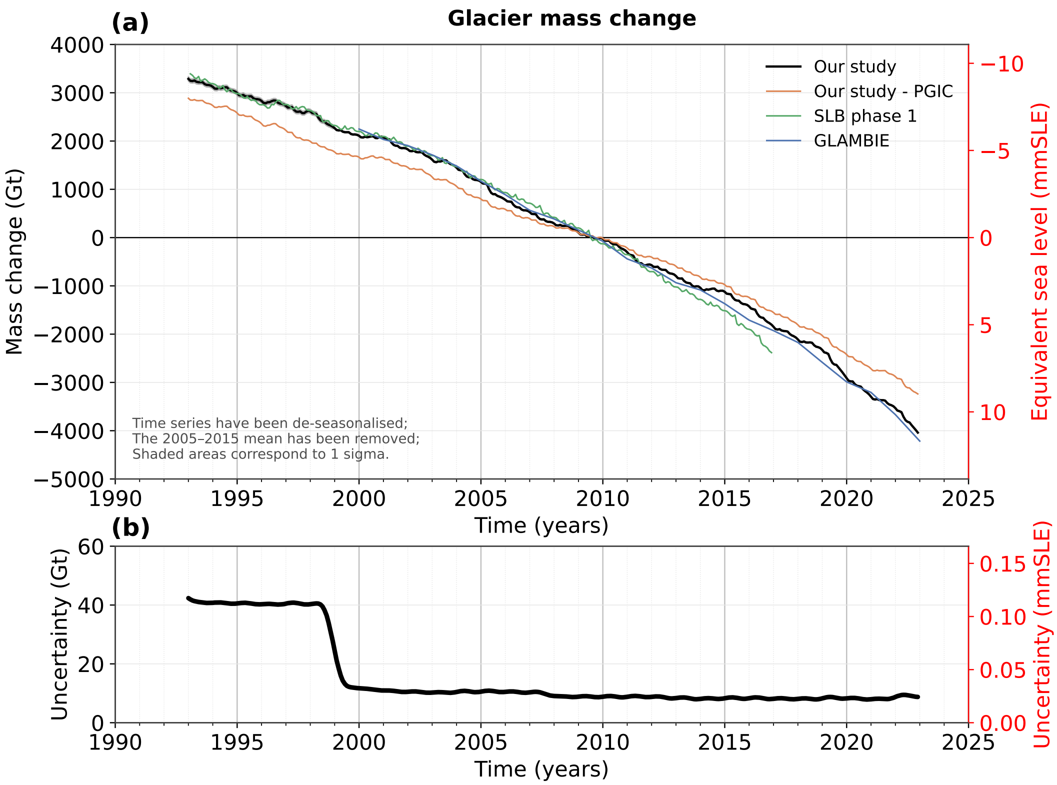

Figure 5. The cumulate GIC mass change and their contribution to sea-level: (a) data used in the first SLB assessment (Horwath et al., 2022) (green), GLAMBIE community values (Zemp et al., 2025) (blue). Black is the dataset used with $1-\sigma$ uncertainty envelop in this study and the orange curve is for the dataset used here but excluding PGIC. (b) Uncertainties assessed for the estimates in (a)

3.5.2 Uncertainty assessment

The two-sigma uncertainties were calculated by following the approach in Dussaillant et al. (2024) and assumed to be correlated spatially but not temporally due to the way the data set was constructed. The three main error sources in the combination

https://doi.org/10.5194/essd-2026-627
Preprint. Discussion started: 19 August 2026

approach such as elevation change (dh/dt), density conversion of the volume change, and annual mass balance anomaly- are all spatially correlated and propagated accordingly (Dussaillant et al., 2024). For further details of the error assessment and validation see Dussaillant et al. (2024). The period with the highest accuracy in elevation change from DEM differencing is from 2000-2024 and as a consequence, the integrated uncertainty is lowest for this epoch at about $\pm$ 10 $Gt\ yr^{-1}$ at 1-sigma ($\pm$ 0.03 $mm\ yr^{-1}$). Prior to 2000, satellite-based estimates of mass balance are limited and the uncertainties are, consequently, significantly larger at $\pm$ 40 $Gt\ yr^{-1}$ ($\pm$ 0.12 $mm\ yr^{-1}$) (figure 5b). We also compare our GIC times series against the consensus ensemble estimate from the GLAMBIE study Zemp et al. (2025) in figure 5a. It should be noted that both data sets rely heavily on the ASTER Dem differences in Hugonnet et al. (2021) and are not, therefore, independent. Nonetheless, it is evident that there is good agreement between the two. We also compare with the GIC time series used in the ESA SLB phase I study (Horwath et al., 2022), which is marginally more positive over the common period by about 1 mm for a cumulative total of 15 mm from 1992-2017. We do not correct for glacier melt not reaching the ocean due to the role of endorheic basins and evapotranspiration. The magnitude of this has been estimated at 5-6% of the total GIC melt (Rounce et al., 2025) with the majority of this “loss” to the ocean coming from the High Mountains Asia (the Himalaya primarily), where it is about 30% of the total melt for the region. This represents an absolute value of about 15 $Gt\ yr^{-1}$ or 0.04 $mm\ yr^{-1}$. It should be noted that there are other potential cryospheric sources of mass to the oceans such as Arctic permafrost thaw, which are not considered here.

3.6 Greenland and Antarctica’s ice sheet mass change

We use two published datasets for ice sheet mass balance, namely the aggregated assessment by the Ice-sheet Mass Balance Intercomparison Exercise (IMBIE) and the Gravimetric Mass Balance (GMB) products by the Greenland Ice Sheet CCI and Antarctic Ice Sheet CCI projects.

The latest IMBIE assessment (Otosaka et al., 2023) compiled a total of 27 contributed mass balance assessment for GIS (23 for the AIS), comprising assessments from each of the major approach (altimetry, gravimetry, Imput-Output Method). This aggregated assessment was an instrumental source for the IPCC AR6 assessment of ice sheets’ sea-level contribution. The time span covered is 1992-01 to 2020-12.

The gravimetric mass balance (GMB) products generated at TU Dresden within the GIS_cci+ and AIS_cci+ projects (Döhne et al., 2023; Groh and Horwath, 2021, https://data1.geo.tu-dresden.de) are based on the analysis of GRACE and GRACE-FO L2 gravity field solutions. They have been validated within these two CCI projects and similar CCI GMB products were used in the sea-level budget analysis by Horwath et al. (2022). The time span covered is 2002-04 to 2024-02.

3.6.1 Methods and product

The IMBIE time series of mass change estimates are aggregated as documented in detail by Otosaka et al. (2023). The aggregation is in two steps: first among assessments following the same of the three approaches, and second across the three approaches. Each aggregation applies a weighting accounting for assessed uncertainties. The published dataset comprises time series from 1992-01 to 2020-12 at a monthly resolution of mass balance and its uncertainty (Gt/yr) as well as cumulative mass

https://doi.org/10.5194/essd-2026-627
Preprint. Discussion started: 19 August 2026

balance (since 1992-01) and its uncertainty (Gt). While the formal temporal resolution of the aggregated dataset is monthly, the effective temporal resolution of some of the input assessments (notably from altimetry) is coarser, so that the time series are unlikely to reflect the full month-to-month variability of mass balance.

The CCI GMB products include a monthly gridded product and a monthly basin-integral mass change product. The underlying methodology (Döhne et al., 2023; Groh and Horwath, 2021) is similar (a methodological predecessor) to the methodology described in Section 3.3. The time series contains mass anomalies w.r.t. 2011-01-01 (according to the 2011-01-01 value of a functional fit to the period 2002-08 - 2016-08). Different GIA models are applied in the GIA correction for the two ice sheets: the model IJ05_R2 (Ivins et al., 2013) for the AIS, and the weighted ensemble mean GIA solution by Caron et al. (2018) for Greenland without ensuring the global consistency of both GIA products.

In this study, the ice sheet mass change time series are constructed by concatenating the IMBIE product for the period January 1993 to December 2020 with the CCI GMB datasets covering 2021–2022 separately for the Greenland and Antarctic ice sheets. The two datasets are merged by estimating their mean offset over the overlapping year 2020. This offset is then removed from the CCI GMB time series, which is first low-pass filtered using a 2-year filter to ensure consistency with the IMBIE product. The resulting Greenland and Antarctic ice sheet mass change time series are presented in Figures 6 and 7, respectively (black curve in panel a).

3.6.2 Uncertainty assessment

The IMBIE formalism detailed by Otosaka et al. (2023) propagates uncertainties from the contributed assessment through the aggregation procedure. Since the cumulative mass balance is w.r.t. the start of the time series in 1992-01, given uncertainties are also w.r.t. this starting time and consequently increase monotonically in time. Uncertainties of cumulative mass anomalies w.r.t. a different reference time can be generated by cumulating the uncertainties of the mass balance rates w.r.t. the new reference time. The methodology of aggregating mass balance uncertainties in time does not consider temporal correlations of the monthly mass balance uncertainties. This limits the ability to reflect systematic uncertainties such as the GIA-related uncertainty of gravimetric estimates or firn-density related uncertainties and spatial-sampling related uncertainties for altimetric estimates.

For the CCI GMB products, uncertainties of the monthly mass anomalies are modelled as the combined effect of uncertainties of the temporal linear trend, σ^2_{trend}, and a temporally uncorrelated noise, σ_{noise}. The uncertainties of linear trends are summed up in quadrature from uncertainties due to different error sources (b, c, d outlined in Section 3.3.2). The trend uncertainties are given separately. In this way, it can be propagated to monthly uncertainties w.r.t. a reference time of the user's choice. The error variance at any epoch is then $\sigma^2_{total}(t) = \sigma^2_{noise} + \sigma^2_{trend}(t - t_0)^2$. While the CCI GMB methodology attempted to separate mass changes of the proper ice sheet from mass changes of peripheral glaciers, the limited sensitivity of GRACE and GRACE-FO to spatial scales smaller than 200 km (in polar regions), limits the fidelity of this separation, a problem that is commonly expressed as leakage effect.

https://doi.org/10.5194/essd-2026-627
Preprint. Discussion started: 19 August 2026

For this study, the uncertainty provided on the ice sheet datasets are derived from the IMBIE assessment. According to Table 2 in Otosaka et al. (2023), the uncertainty in the mean mass loss trend over the period 1993–2022 is 18 $Gt\ yr^{-1}$ for Antarctica and 16 $Gt\ yr^{-1}$ for Greenland.

Figure 6 and 7 compare the IMBIE aggregated assessment and the CCI GMB assessments with each other for Greenland and Antarctica respectively. In addition, we compare these two assessments with the ice sheet mass balance assessments used by the first SLBC_cci project (SLBC-1) (Horwath et al., 2022). SLBC-1 used two alternative ice sheet assessments: one from gravimetry and one from altimetry. All time series show a very similar long-term behavior, e.g., for Greenland, with an acceleration of mass loss between 1995 and 2012 and some deceleration around 2012. Differences occur w.r.t. the short-term signals. While seasonal signal is visible in the CCI GMB time series (in particular for the GIS), seasonal signals were removed from the SLBC-1 GRACE-based time series and are not present in the IMBIE and SLBC-1 altimetry-based time series owing to their effective temporal resolution of 3 years and 3 to 5 years, respectively. This difference in temporal resolution also explains the smoother appearance of the IMBIE and altimetry-based time series. The GRACE time series for the AIS exhibits a notable month-to-month noise component, partly related to the uncertainties of low-degree spherical harmonic components of the underlying gravity field solutions. The altimetry-based SLBC-1 time for series for the AIS is a monthly interpolation of an originally 140-day resolution.

https://doi.org/10.5194/essd-2026-627
Preprint. Discussion started: 19 August 2026

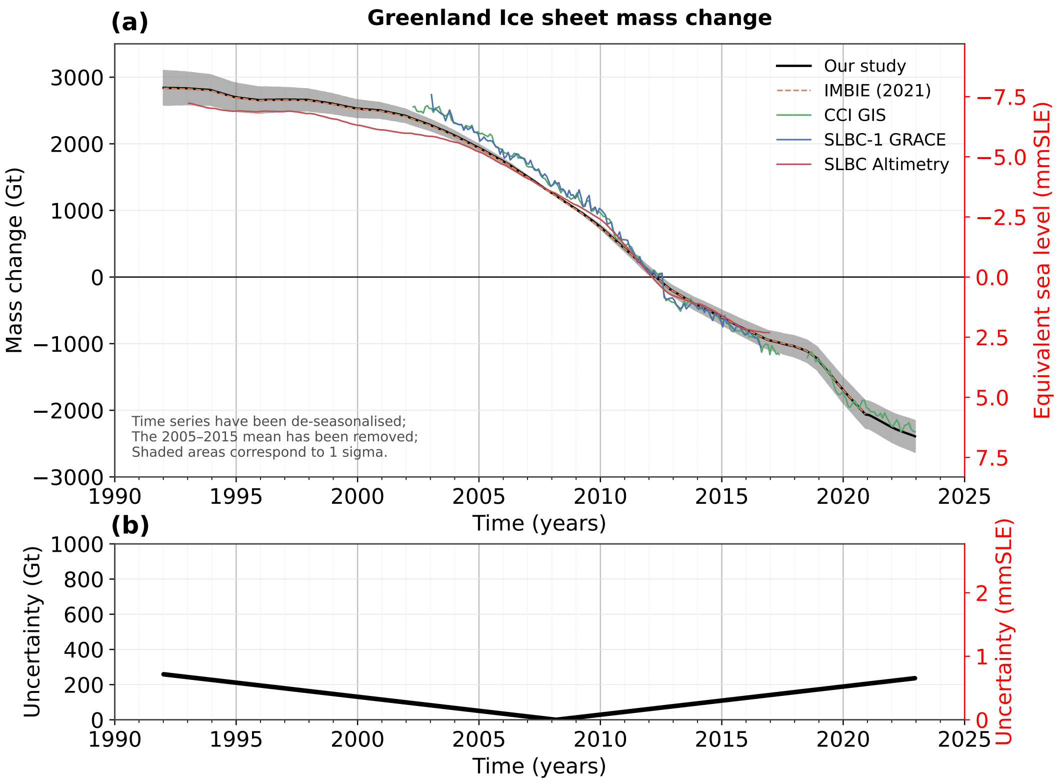

Figure 6. Mass changes of the Greenland Ice Sheet: (a) comparison of IMBIE assessment (dotted orange), the GIS_cci+ Gravimetric Mass Balance (GMB) assessment (green, RL4.1), the GRACE-based assessment used by the first SLBC_cci project (blue) and the altimetry-based assessment used by the first SLBC_cci project (red). Black curve is the dataset used in this study with $1-\sigma$ uncertainty envelop; (b) Uncertainties assessed for the estimates in (a)

https://doi.org/10.5194/essd-2026-627
Preprint. Discussion started: 19 August 2026

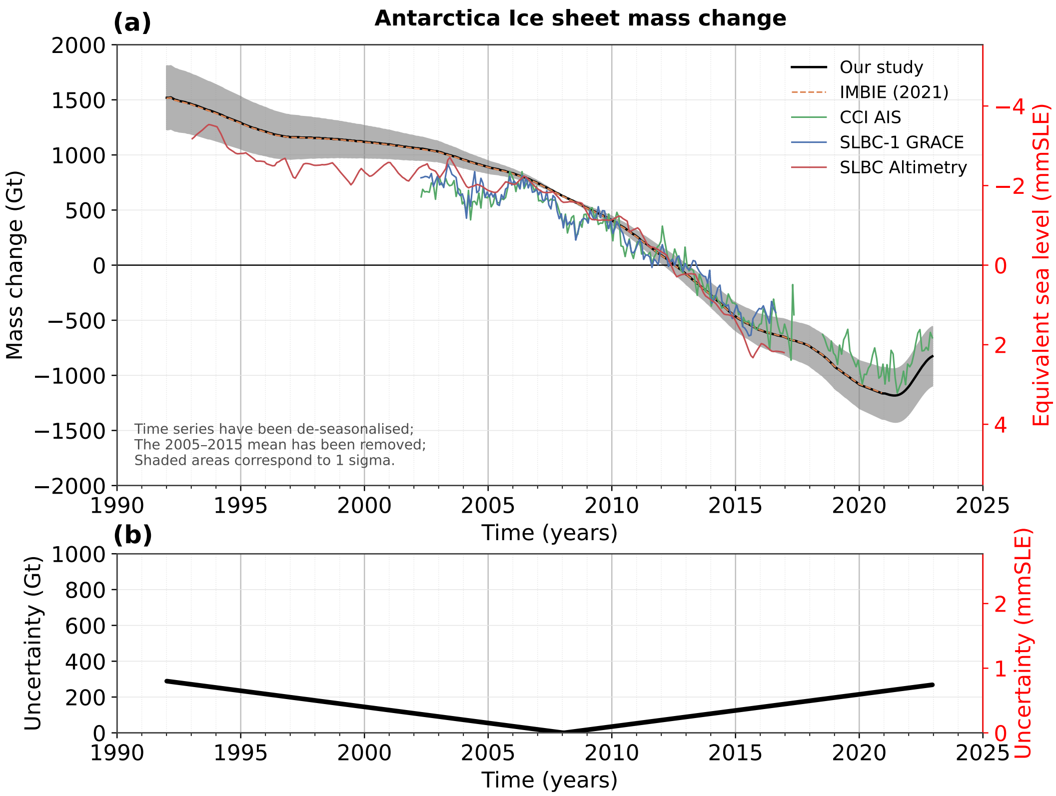

Figure 7. Mass changes of the Antarctic Ice Sheet: (a) comparison of IMBIE assessment (dotted orange), the AIS_cci+ Gravimetric Mass Balance (GMB) assessment (green, RL5.0), the GRACE-based assessment used by the first SLBC_cci project (blue) and the altimetry-based assessment used by the first SLBC_cci project (red). Black curve is the dataset used in this study with $1-\sigma$ uncertainty envelop; (b) Uncertainties assessed for the estimates in (a)

Table 5 quotes mean linear trends over the common period of the four time series (from 2003-01 to 2016-08). For the GIS, the spread is slightly larger than the uncertainty quoted for the individual assessments. Part of the differences likely arises from the different degrees of inclusion of peripheral glaciers. Their contribution is partly included in the GRACE-based assessment, while it is not included in the altimetry-based assessments used here. Hugonnet et al. (2021) estimate the peripheral glacier mass change between 2000 and 2019 on the order of -35 Gt/yr. For the AIS, the range of the trends between -98 Gt/yr and -135 Gt/yr reflects the well-known spread among results from different techniques (and even from different realisations of the same techniques). Uncertainties quoted for the gravimetric results are in line with this spread, while uncertainties quoted for IMBIE and SLBC-1 altimetry are smaller.

https://doi.org/10.5194/essd-2026-627
Preprint. Discussion started: 19 August 2026

Open Access Earth System Science Data Discussions

Table 4. Mean linear trends of ice sheet mass over the period 2003-01 – 2016-08 for the GIS and the AIS from the four assessments shown in Fig. 6 and 7. Uncertainties are quoted from the data sources. In the case of the IMBIE assessment, uncertainties are calculated from the uncertainties quoted by Otosaka et al. (2023) for three consecutive 5-year intervals under the assumption of uncorrelated errors, in line with the uncertainty aggregation approach of IMBIE.

	GIS [Gt/yr]	AIS [Gt/yr]
IMBIE	-253 ± 16	-135 ± 18
CCI GMB	-282 ± 14	-98 ± 44
SLBC-1 GRACE	-281 ± 8	-102 ± 40
SLBC-1 Altimetry	-246 ± 22	-125 ± 14

3.7 Land water storage mass change

The land water storage (LWS) mass change encompasses mass change from various water reservoirs over land: snow, canopy, soil moisture, groundwater, lakes, reservoirs, wetland and rivers. The term LWS excludes glaciers and ice sheets already addressed in a dedicated contribution (see Section 3.5 and 3.6). LWS variations are due both to natural variability (climate-driven contribution) and to anthropic activities (anthropogenic or human-induced contribution). The climate-driven contribution mainly drives seasonal and inter-annual variations, without any strong long-term trend. Concerning the human-induced contribution, while it was negligible over the 20th century (i.e. over the 1900s), it has been increasingly important over the last decades, reaching a contribution of about $0.37\ mm\ yr^{-1}$ over 2003-2016 (Cáceres et al., 2020).

The LWS component has been estimated using three hydrological models: GRACE-REC, ISBA-CTRIP and WGHM (Figure 8a). GRACE-REC model is an estimate of the climate-driven LWS based on precipitation and calibrated against GRACE data (Humphrey and Gudmundsson, 2019) using three climate forcing models (ERA5, GSWP3 and MSWEP) and two GRACE datasets (from GSFC and JPL). Depending on the climate forcing model GRACE-REC products are vailable from 2002 until 2014, 2016 and 2019 (GSWP3, MSWEP and ERA5 respectively). These estimates based on precipitations include the contribution of land ice. ISBA-CTRIP (Interaction Soil-Biosphere-Atmosphere, Total Runoff Integrating Pathways) hydrological model provides estimates of LWS until the end of 2018 (Decharme et al., 2019). The Water Global Assessment and Prognosis (WaterGAP) Hydrological Model (WGHM) version 22e (Müller Schmied et al., 2024) provides estimates of LWS using ERA5 and W5E5 datasets for climate forcing, with and without the anthropogenic contribution. The W5E5-based data are provided until the end of 2019 while the ERA5-based data are provided until the end of 2022.

3.7.1 Methods and product

Global mean LWS variations were obtained by spatially averaging the gridded LWS fields over land areas excluding Greenland, Antarctica and glacier areas (Figure 8a). Different climate-forcings can lead to significantly different hydrological model outputs explaining the spread among LWS estimates during the first decade (Müller Schmied et al., 2021). However, the agreement among the different estimates improved markedly after 2004. There is currently no scientific consensus regarding

https://doi.org/10.5194/essd-2026-627
Preprint. Discussion started: 19 August 2026

Open Access Earth System Science Data Discussions

the most suitable climate-forcing dataset. In this study, we made the choice to use the average between the 2 WGHM time series forced by ERA5 and W5E5 climate-forcings (blue and orange curve in figure 8a) to estimate the LWS variation.The uncertainty associated with this choice (see section 3.7.2) is accounted for through the spread among the different climate-forcing (Figure 8a and Figure 8b). This choice is motivated by the fact that, from 2004 onwards, all the models are consistent; furthermore it ensures the consistency of the time series across the entire study period. Moreover, the selected hydrological model ensures the availability of an LWS time series extending over the most recent period, while maintaining continuity with the approach adopted in the previous ESA CCI assessment by (Horwath et al., 2022).

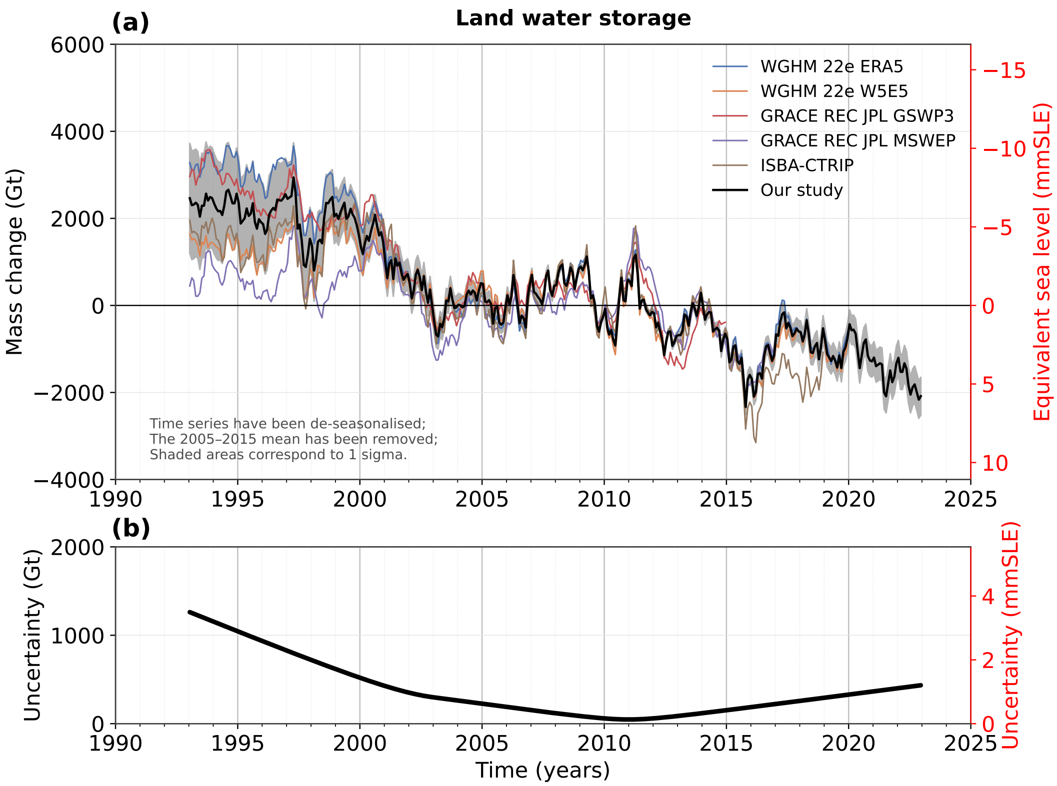

Figure 8. Land water storage (LWS) contribution to sea-level change: (a) comparison of WGHM22e, forced by the ERA5 (blue curve) and W5E5 (orange curve) climate datasets, GRACE-REC estimates constrained by JPL GRACE data and forced by the GSWP3 (red curve) and MSWEP (purple curve) climate datasets, the ISBA-CTRIP hydrological model (brown curve). The black curve represents the LWS component used in this study with $1-\sigma$ uncertainty envelop; (b) Uncertainties assessed for the estimates in (a).

3.7.2 Uncertainty assessment

The estimation of the LWS uncertainty is based on the analysis of the differences between the two WGHM time series used. The uncertainties have been modelised into an uncertainty budget with different sources following the methodology in altimetry (Ablain et al., 2019; Guérou et al., 2023).

https://doi.org/10.5194/essd-2026-627
Preprint. Discussion started: 19 August 2026

First, uncertainties associated with differences in LWS estimates arising from different climate forcings used in the WGHM (ERA5 and W5E5) were characterized and modeled. The uncertainties are modeled by separating the spectral content of the differences between the WGHM-simulated contributions relative to the average (not shown). Differences were separated into 2 different noise error signals correlated at 6 months and 3 years and a drift error signal. Temporal structure of errors has been modelised with a short-term time correlated effect at 6 months of 0.13 mm. Also, a second long-term time correlated effect of 0.13 mm has been modelised for 1993–2008. Then, a linear time correlated effect over the period 1993–2003 of 0.3 $mm\ yr^{-1}$ (table 5) has been modelised.

Second, we consider the uncertainty associated with the anthropogenic contribution to LWS. We adopt the uncertainty range reported by Cáceres et al. (2020) for the trend in the human-induced LWS contribution over the period 1976–2002. Although this period does not exactly coincide with our study period (1993–2022), the time spans are comparable. The estimated trends range from 0.14 to 0.25 $mm\ yr^{-1}$, and the spread of these estimates (0.11 $mm\ yr^{-1}$) is adopted as the standard uncertainty of the anthropogenic LWS trend (Table 5).

Table 5. Temporal structure of uncertainty estimations for land water storage component.

Source of uncertainty	**Temporal structure**	**Standard uncertainty u at 1-sigma**
Climate forcings	Short-term time-correlated effects at 6 month	$u = 0.13$ mm
	Long-term time-correlated effects at 3 years	$u = 0.13$ mm
	Linear time-correlated effect (drift) over period 1993-2003	$u = 0.3\ mm\ yr^{-1}$
Anthropogenic contribution (Cáceres et al., 2020)	Linear time-correlated effect (drift) over period 1993-2022	$u = 0.11\ mm\ yr^{-1}$

Table 5 summarises all the different sources of uncertainties related to the LWS component and their temporal structure. The combination of all these sources of uncertainties can therefore be used to provide a variance covariance matrix of the LWS component. This matrix is used to estimate the uncertainty in the trend of LWS for any period length and time, based on the extended OLS approach. The period of reference used for the computation of uncertainties is 2005-2015 included. In other words, the uncertainty relates to the variations of LWS with respect to the average of LWS over 2005-2015. The variance covariance matrix is used to estimate the 1-sigma uncertainty envelope shown in figure 8a and b.

3.8 Atmospheric water vapor mass change

The Atmospheric water vapor mass change at global scale is proportional to the mean surface temperature related by Clausius Clapeyron equation. This atmospheric water vapor is commonly referred to as total column water vapor (TCWV) or precipitable water. This contribution is estimated to about -0.04 $mm\ yr^{-1}$ over 1993-2015 by Dieng et al. (2017) and to about -0.08 $mm\ yr^{-1}$ over 2005-2018 by Barnoud et al. (2023a) based on ERA5 data.

https://doi.org/10.5194/essd-2026-627
Preprint. Discussion started: 19 August 2026

3.8.1 Methods and product

In this study, we use the ERA5 monthly quarter degree resolution TCWV dataset (Hersbach et al., 2023). This dataset is available from 1993 until present. To estimate the atmosphere water vapor content, the TCWV data are summed over the whole globe and expressed in Gt. the product used in this study compares well with an independent estimate is made using the ESA CCI estimates over land combined with the Hambourg Ocean-Atmosphere Fluxes and Parameters from Satellite (HOAPS) data over oceans (see Figure 9a).The availability of this combined dataset is limited to 2002-2017 due to the time range of the CCI dataset.

In agreement with the increase in surface temperature, atmospheric water vapor is increasing since 1993 to 2024 and presents important inter-annual variations especially during ENSO events (see Figure 9).

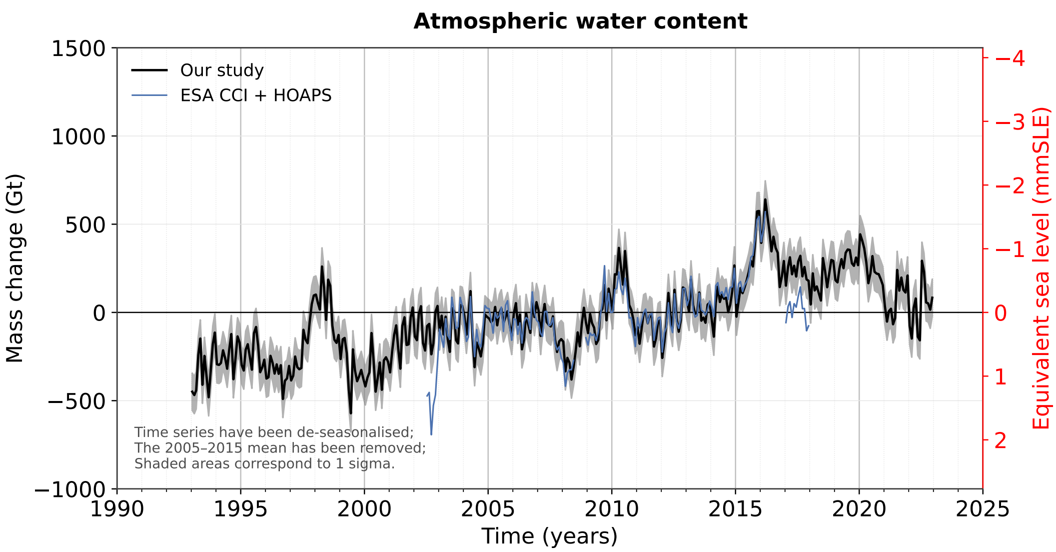

Figure 9. Atmospheric water vapour content change contribution to global mean sea-level change: comparison of ESA CCI dataset over land combined with the HOAPS data over oceans (blue), balck curve represents the component used in this study with $1-\sigma$ uncertainty envelop.

3.8.2 Uncertainty assessment

To obtain an uncertainty estimate on the atmospheric water vapor mass change, the ERA5 estimates is compared to other estimates. Over the common period between ERA5 and CCI+ HOAPS estimates, the standard deviation of the difference is computed and used as standard uncertainty of a white noise uncertainty for the atmosphere water vapor contribution. This white noise is estimated at $0.29\ mm$ on a monthly basis.

https://doi.org/10.5194/essd-2026-627
Preprint. Discussion started: 19 August 2026

4 Global water mass budget

The Global water mass budget, also known as ocean mass budget, is assessed by comparing two independent estimates of the barystatic sea-level. The first estimate is derived directly from satellite gravimetry (GRACE and GRACE-FO), providing a direct measurement of ocean mass change. The second estimate is obtained by summing the individual mass contributions from the various reservoirs of the climate system, as defined in Equation 3.

Barystatic sea-level trend is dominated by glacier mass change (including peripheral glaciers), Greenland and Antarctic ice sheets mass change (See Figure 10) . Over the P2 period (gravimetry era, see Table 6), these components exhibit significant positive trends of $0.74 \pm 0.01\ mm\ yr^{-1}$, $0.67 \pm 0.04\ mm\ yr^{-1}$, and $0.33 \pm 0.04\ mm\ yr^{-1}$, respectively. On the other hand, land water storage mass change (teal line) is responsible for most of the interannual variability and to a lesser extent to the long-term trend of $0.27 \pm 0.09\ mm\ yr^{-1}$. Finally, the atmospheric water vapor component (pink line) represents the smallest contribution, with a slight negative trend of -0.05±0.01 mm yr^{-1} showing that atmosphere is storing more water over the recent period.

During the 2004–2015 period, a good agreement is observed between the two independent estimates, indicating a successful closure of the ocean mass budget within the GRACE mission's early stages. However, significant discrepancies emerge after 2015 (see figure 10b). Between late 2015 and early 2016, a high-amplitude signal is clearly visible in the gravimetry-based barystatic sea-level (Fig. 10a, dark blue line) which is not fully observed in the GWB-based barystatic sea-level (Fig. 10a, light blue line). This mismatch results in a marked jump in the budget residuals (Fig. 10b). This inconsistency suggests a potential underestimation of a rapid mass signal within the individual components, most likely linked to an unresolved or underestimated contribution from Land Water Storage during this specific inter-annual event. The pronounced LWS anomaly observed during 2015–2018 closely matches the corresponding anomaly in the barystatic sea-level record, further supporting the interpretation that this event is predominantly associated with variations in land water storage.

During the GRACE-FO era (2018–present), the budget no longer closes, with the residuals showing a significant and persistent trend. This divergence may reflect either a missing barystatic contribution from the global water budget, corresponding to an accumulated signal of nearly 10 mm over the study period, or residual errors in the GRACE-FO observations. Differences between different gravimetry-based barystatic time series (Fig. 4) show interannual patterns similar to the interannual pattern of the mass budget residuals (Fig. 12), although with smaller amplitude. For example, the difference GSFC minus 'our study' is negative in 2016 at a level of -1 mm, it is small in 2019-2020 and it rises to a level of 1 mm after 2021. This observation may suggest that part of the mass budget residuals is due to issues with the GRACE/GRACE-FO data and data analysis, which are reflected differently in different gravimetry-based solutions.

https://doi.org/10.5194/essd-2026-627
Preprint. Discussion started: 19 August 2026

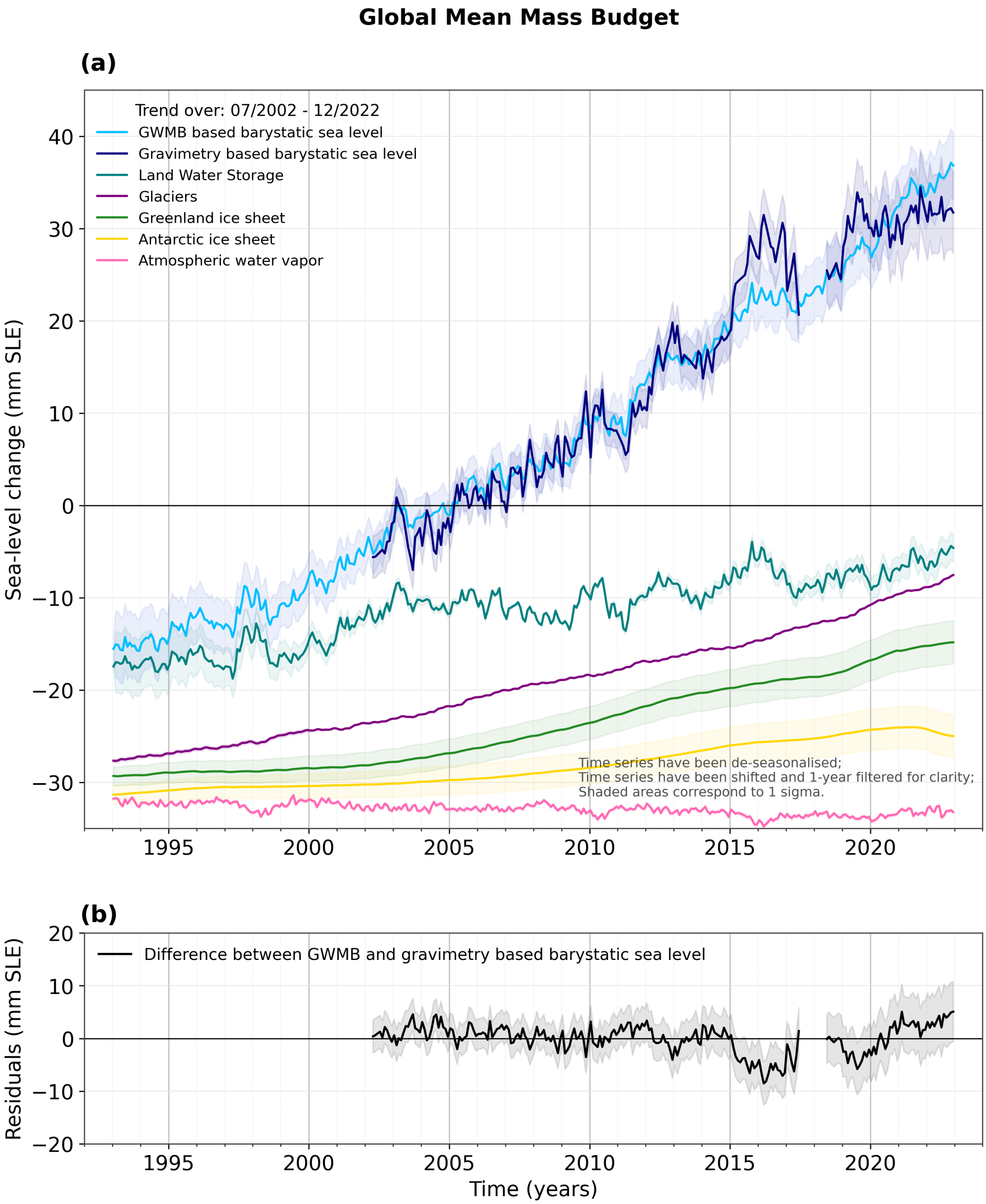

Figure 10. a) Global mean barystatic sea-level time series for SLBC CCI+. Blue lines show the total barystatic component: dark blue for barystatic from GRACE/GRACE-FO data, and light blue for barystatic from the sum of individual mass components. The rest of the components are Land water storage (teal line), glacier (purple line), Greenland Ice Sheet (green line), Antarctic Ice Sheet (yellow line) and atmospheric water vapor (pink line). (b) Difference between GMWB-based and gravimetry-based barystatic sea-level or residuals. Trends are estimated over the period 06/2002 - 12/2022.

https://doi.org/10.5194/essd-2026-627
Preprint. Discussion started: 19 August 2026

Open Access Earth System Science Data Discussions

5 Sea-level budget

5.1 Global Scale

5.1.1 Direct approach

The sea-level budget (SLB) at global scale is evaluated using Eq. 2 by comparing the altimetry-based relative sea-level (RSL) against the sum of the thermosteric sea-level and both barystatic sea-level (described in section 4). Note that in this paper, a consistent mask has been applied to all datasets defined in section 2.1.

Focusing on the SLB residuals, there are three distinct behaviors over three successive periods: 1993–2003, 2004–2014, and 2015–2022. During the first period (1993–2003), when the barystatic contribution relies exclusively on individual mass components because satellite gravimetry was not yet available, the residuals display substantial interannual variability (see Figure 11b, red line). Nevertheless, the estimated trend over this period ($-0.08\ mm\ yr^{-1}$) is not statistically significant given its uncertainty ($0.73\ mm\ yr^{-1}$). Several factors may explain this enhanced variability. First, thermosteric sea-level estimates are less reliable before the Argo era and rely primarily on XBT and CTD observations. This leads to important variability in the different estimates as shown in Figure 3b. Second, as discussed in Section 3.2, discrepancies also exist among the available altimetry products during the TOPEX era. Finally, the land water storage (LWS) variations are also comparatively large, with substantial differences among the available LWS datasets (section 3.7).

https://doi.org/10.5194/essd-2026-627
Preprint. Discussion started: 19 August 2026

Open Access Earth System Science Data Discussions

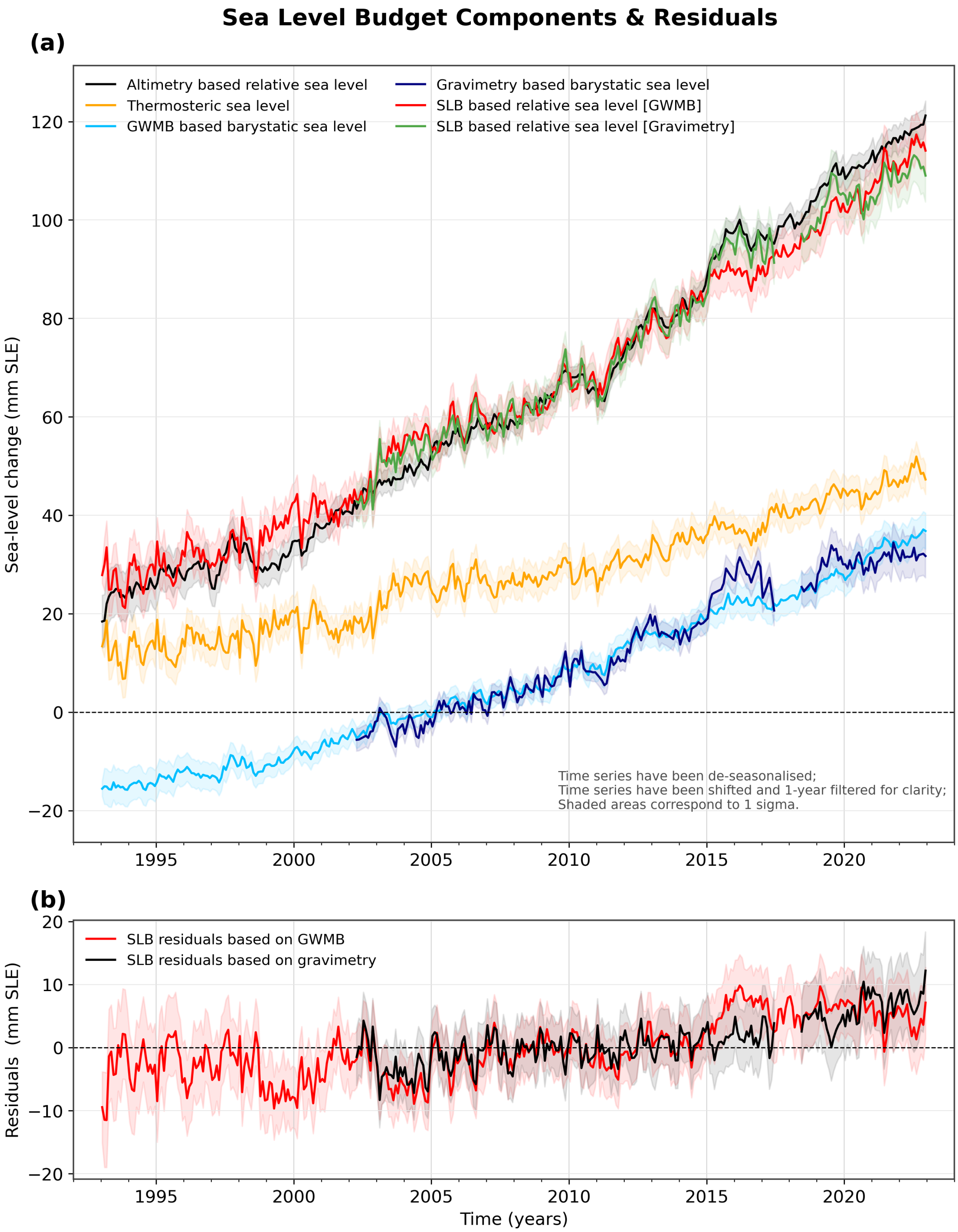

Figure 11. Global-mean Sea-level budget components (a) and residuals (b). Altimetry-based relative sea-level (black curve) is compared to SLB-based relative sea-level derived from gravimetry (green) and from GWMB (red); Components as thermosteric contribution (orange), and Barystatic sea-level from GWB (light blue) and gravimetry (dark blue) are shown for comparison. (b) Residuals of the sea-level budget, computed as the difference between the altimetry-based relative sea-level and the SLB based relative sea-level when using barystatic from GWMB (red line) and gravimetry (black curve).

https://doi.org/10.5194/essd-2026-627
Preprint. Discussion started: 19 August 2026

The sea-level budget also closes remarkably well during the period 2004-2014, which corresponds to the period during which the global water mass budget (GWMB) exhibits also its best closure (section 4). Using the gravimetry-based estimate of barystatic sea-level, the residual trend is estimated at $0.35 \pm 0.45\ mm\ yr^{-1}$ and is therefore not statistically significant. When the GWMB-based barystatic estimate is used, the residual trend increases slightly to $0.46 \pm 0.36\ mm\ yr^{-1}$ and remains statistically significant. However, the uncertainties associated with the GWMB mass components are likely underestimated relative to those derived from satellite gravimetry, which calls into question the significance of this residual trend and highlights the need for further improvements in the GWMB-based uncertainties estimation. Overall, this updated assessment confirms the conclusions of Horwath et al. (2022).

In contrast, during 2015–2022, the sea-level budget residuals exhibit a significant positive trend using both barystatic estimates. However, the temporal evolution of the residuals differs between the two approaches (Figure 11b). The gravimetry-based residuals display an approximately linear increase ($1.00 \pm 0.57\ mm\ yr^{-1}$), whereas the GWMB-based residuals are characterized by an abrupt step of almost 10 mm from 2015 to 2016 followed by a non-significant trend ($-0.19 \pm 0.48\ mm\ yr^{-1}$). Since the GWMB also fails to close over this period, this discrepancy raises questions regarding the accuracy of the barystatic estimates during the most recent years. Further investigation is required to identify the origin of these discrepancies and to assess their impact on long-term sea-level budget closure.

Over the full study period (P2), Satellite altimetry measures a mean RSL rise of $3.86\ mm\ yr^{-1}$, of which approximately $1.3\ mm\ yr^{-1}$ is explained by thermosteric sea-level and about $2.0\ mm\ yr^{-1}$ by the barystatic contribution (Table 6), with residual trends of $0.58 \pm 0.26\ mm\ yr^{-1}$ when using the GWMB estimate and $0.52 \pm 0.36\ mm\ yr^{-1}$ when using satellite gravimetry. For period P1, the residual trend reaches $0.39 \pm 0.28\ mm\ yr^{-1}$ using the GWMB estimate. In all cases, the residual trends remain statistically significant over the corresponding analysis periods.

https://doi.org/10.5194/essd-2026-627
Preprint. Discussion started: 19 August 2026

Table 6. Trends estimation and corresponding uncertainties of sea-level and global water budgets components and residuals estimated over P1 (1993–2022) and P2 (2004–2022) using the direct and the objective approaches. Trends are expressed in $mm\ yr^{-1}$

Variable in $mm\ yr^{-1}$	**Direct approach Trend over P1 (1993–2022)**	**Direct approach Trend over P2 (2004–2022)**	**Objective approach Trend over P2 (2004–2022)**
Altimetry based relative sea-level	3.39±0.20	3.86 ± 0.18	3.85±0.16
Thermosteric sea-level	1.24±0.14	1.32 ± 0.15	1.32±0.19
Gravimetry-based barystatic sea-level		2.02 ± 0.28	2.55±0.17
GWMB-based barystatic sea-level	1.77±0.01	1.95 ± 0.01	
Land water storage	0.38±0.13	0.27 ± 0.09	
Glaciers	0.65±0.01	0.74 ± 0.01	
Greenland ice sheet	0.53±0.04	0.67 ± 0.04	
Antarctic ice sheet	0.26±0.04	0.33 ± 0.04	
Atmospheric water vapor	−0.05 ±0.01	-0.05 ± 0.01	
SLB residuals based on gravimetry		0.52 ± 0.36	0.00±0.25
SLB residuals based on GWMB	0.39±0.28	0.58 ± 0.26	

Long-term trends previously described in the residuals emerge from specific errors occurring at some precise time toward the end of the time series which then propagate in the trend estimate especially if the period over which the trend is computed starts or ends at this specific time (see Figure 12). This feature points toward particular instrument issues located in time in 2015 (in the SLB using the GWMB) or 2018 and 2020 (in the SLB using satellite gravimetry). More generally the sea-level budget residuals also consistently exhibit low-frequency variations, which remain an open question and may reflect inconsistencies or errors in one or more of the input components.

Furthermore, Figure 12 indicates that ENSO events exert a significant interannual influence on the closure of the sea-level budget, particularly when relying on mass components (panel a). In particular, a major discrepancy between the GRACE/GRACE-FO barystatic time series and the GMWB barystatic estimate arises during the exceptionally strong 2015–2016 El Niño event (Santoso et al., 2017). While the GRACE-based barystatic sea level displays a pronounced, high-amplitude signal spanning a ∼4-year period starting in 2015, this variation is noticeably absent from the GMWB barystatic time series. Given that the LWS component drives most of the interannual variability in the GWMB, we suspect that the LWS model failed to capture the exceptional ocean-land mass transfers associated with this extreme ENSO event.

https://doi.org/10.5194/essd-2026-627
Preprint. Discussion started: 19 August 2026

Open Access Earth System Science Data Discussions

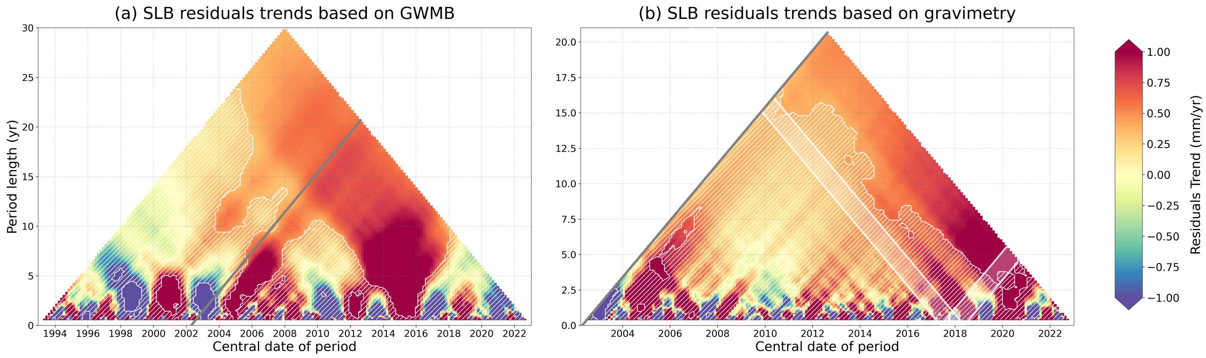

Figure 12. Trend diagram of the SLB residual trend with manometric estimate from mass component (a) and GRACE (b) for any period and at any time. Dashed areas corresponds to non-significant trend compared to its uncertainty. The gray line on panels (a) and (b) marks the start of the GRACE mission, and the transparent white area on panel (b) indicates the gap period between the GRACE and GRACE-FO missions. Note that both axes are different between panels (a) and (b).

5.1.2 Objective closure approach

A significant global trend in the SLB residuals suggests a potential missing or underestimated contribution, as previously shown. To address this, an objective closure approach, based on an inversion method (detailed in Appendix A), was implemented. This approach was applied to the SLB for the period 2004–2022, utilizing the standard components and their associated uncertainties, as detailed in Section 3. We limited the application of this method to the P2 period (2004–2022) because it depends on the uncertainty characterization of the sea-level budget components. Barystatic sea-level uncertainties are reliably quantified only from the onset of satellite gravimetry, and thermosteric sea-level uncertainties become well constrained only after the quasi-global deployment of Argo floats.

The inversion successfully identified an optimal solution that perfectly closes the SLB (Figure 13b), a solution consistent with the estimated uncertainties of each component, although this agreement is on the edge of the [5-95%] CL envelope for the barystatic (see Figure 13 a). Furthermore, this optimization not only achieved budget closure, but also substantially reduced the uncertainties associated with each component in the optimal solution as a result of imposing the closure, which reduces the uncertainty of the most uncertain components to ensure consistency with the uncertainty of the less uncertain components.

The adjustments made by the inverse method varied across the SLB components. For altimetry and gravimetry measurements, the optimal solutions show long-term modifications. This aligns with their error budgets, which is dominated by time-correlated errors. These adjustments resulted in trend modifications: relative sea-level changed from $3.86 \pm 0.18\ mm\ yr^{-1}$ to $3.85 \pm 0.16\ mm\ yr^{-1}$, and barystatic sea-level from $2.02 \pm 0.28\ mm\ yr^{-1}$ to $2.55 \pm 0.17\ mm\ yr^{-1}$ (see last column in Table 6).

In contrast, the optimal solution for the thermosteric sea-level was adjusted over the short-term, which is consistent with its uncertainty budget that is dominated by uncorrelated errors (See figure 13).

https://doi.org/10.5194/essd-2026-627
Preprint. Discussion started: 19 August 2026

This outcome highlights the critical importance of accurately describing component uncertainties, particularly correlated errors, as they significantly influence a component's adjustment. Characterizing time-correlated effects in uncertainties is essential for long-term analyses.

Although the objective method shows the sea-level budget can be closed over 2004-2024 within the described uncertainties, the closure is not reached within the 1σ interval of the ocean mass estimate uncertainty from 2017 onward (See figure 13). The fact that closure is reached out of 1σ means that the sea-level budget is closed with less than a 32% probability since 2017. This indicates there is more certainly an inconsistency in the sea-level budget since 2017, and a continuing effort is needed to understand the causes. The fact that the transition between the GRACE and GRACE-FO missions coincides with this rupture suggests a potential effect influencing gravimetry measurements after this date.

https://doi.org/10.5194/essd-2026-627
Preprint. Discussion started: 19 August 2026

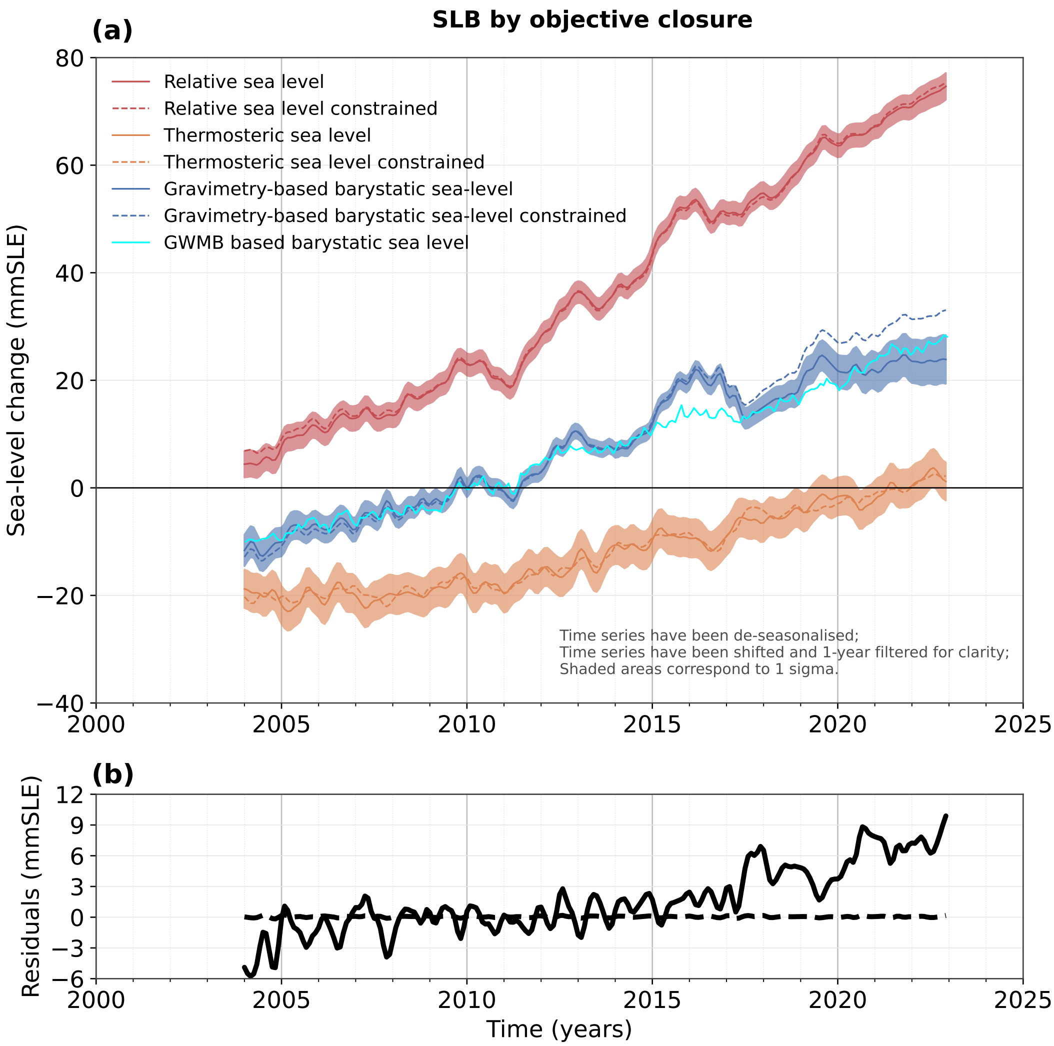

Figure 13. Comparison of various sea-level components. Solid lines represent components derived directly from observations, dashed lines show those obtained through an objectively constrained optimal approach. The panels display: (a) SLB components and (b) SLB residuals.

5.2 Regional scale

Relative sea-level trends are significant over nearly the entire global ocean, with the notable exception of an elongated negative feature east of the Philippines in the western tropical Pacific (see Figure 14a). Regional relative sea-level patterns are predominantly driven by thermosteric variability (see Figure 14 a vs c), a finding consistent with previous studies (e.g., Stammer et al. (2014); Hamlington et al. (2020); Cazenave and Moreira (2022)). In the North Atlantic, thermosteric and halosteric trends exhibit a marked anti-correlation, highlighting the fact that the halosteric component cannot be neglected in regional assessments as it significantly modulates the total steric signal through thermo-halo compensation.

https://doi.org/10.5194/essd-2026-627
Preprint. Discussion started: 19 August 2026

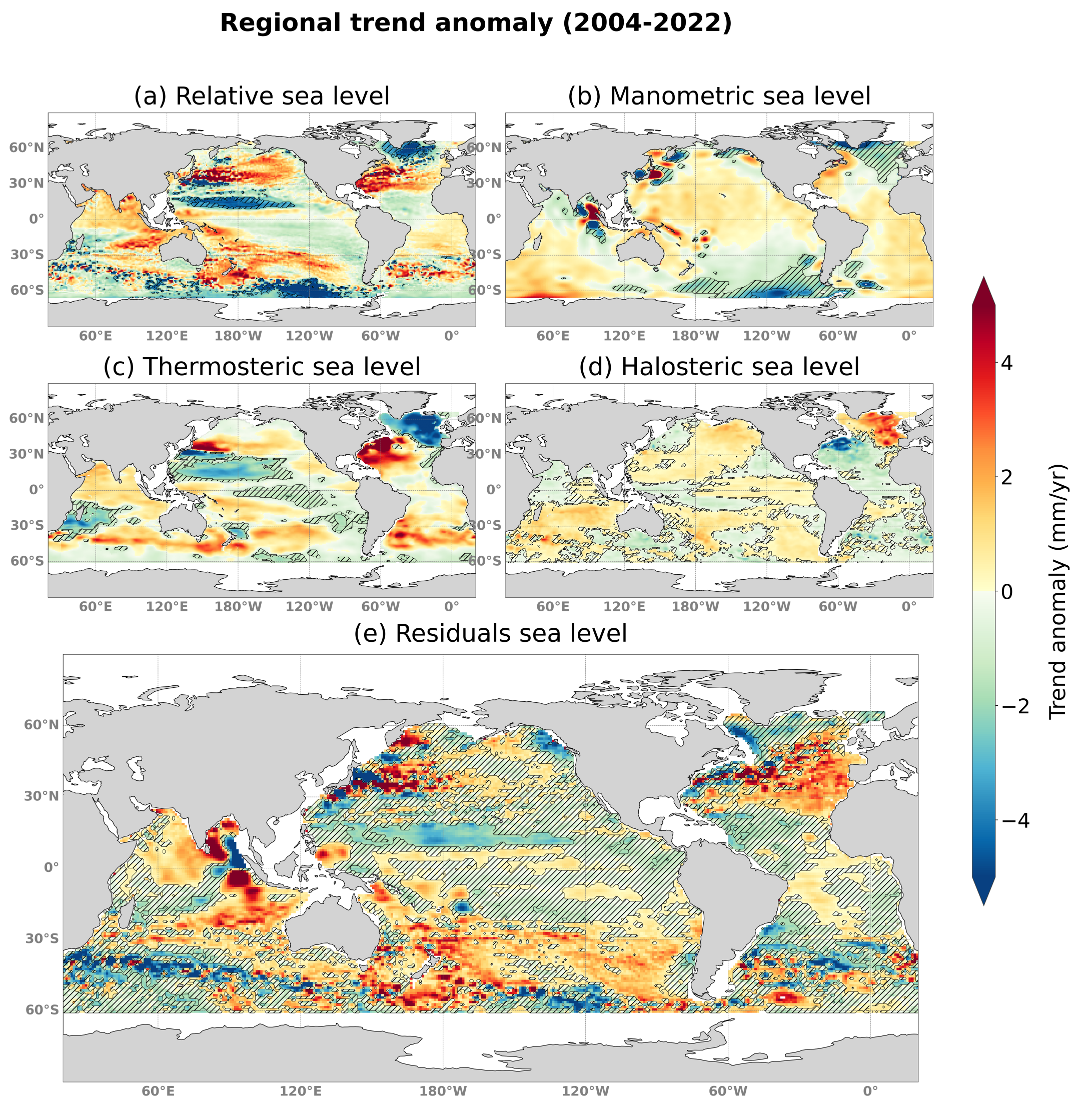

Figure 14. Sea-level regional trend anomalies over January 2004 to December 2022 in observed Altimetry-based relative sea-level (a), Gravimetry-based manometric (b), ARGO-based thermosteric sea-level (c) and ARGO-based halosteric sea-level (d) and budget residual trends (observed sea-level minus sum of components) (e). All figures represent the anomalies with respect each global-mean to highlight the differences. Dashed areas correspond to regions where trends is not significant compared with uncertainties.

Regarding the manometric component, trend are not significant compared with their uncertainties over portions of the North-east Atlantic and the South Pacific. The manometric trend anomaly map is otherwise characterized by large-scale patterns, with positive trends observed across most of the Pacific, the South Atlantic, and the southwestern Indian Ocean. Localized high-amplitude anomalies along the coasts of northern Indonesia and Japan reflect the solid Earth response to the Sumatra (2004)

https://doi.org/10.5194/essd-2026-627
Preprint. Discussion started: 19 August 2026

and Tohoku (2011) earthquakes, respectively, whose corresponding post-seismic signals were not completely removed from the current gravity solutions.

Each observing system samples the ocean at a different effective spatial resolution. Satellite altimetry resolves spatial scales below approximately 100 km, whereas satellite gravimetry and in situ observations are limited to scales of roughly 300 km or large (Chambers et al., 2004; Roemmich and Gilson, 2009). Given these differences in observational resolution, our analysis of the sea-level budget residuals is restricted to spatial scales larger than 300 km.

The residual trend anomaly map (Figure 14e) reveals that, in many regions, the sum of the individual components effectively matches the observed relative sea-level trend anomalies. Across the Pacific and South Atlantic Oceans, the regional sea-level budget is nearly closed within the estimated uncertainties. However, significant large-scale misclosure patterns remain in specific areas, most notably in the North Atlantic and around the Australian continent. Around Australia, the residual patterns closely resemble those of thermosteric sea-level (see Figure 14c and e), suggesting that the ARGO float network is not able to capture the ocean variability around the mesoscale active Antarctic Circumpolar Current and thus the thermosteric sea-level may be underestimated in this region. In contrast, in the North Atlantic, the steric patterns (see Appendix G) do not correspond well with the residual patterns, indicating that a different mechanism is likely responsible.

Recent studies by Bouih et al. (2025); Song et al. (preprint) have investigated these North Atlantic residuals and proposed that they may reflect signals originating from the steric signal in the deep ocean, which is not captured by the Argo observing system. Even though the Deep Argo network has started since a decade to measure the deep ocean layers (notably in the North Atlantic), the density of the measure is for now too sparse to provide an estimate for this study. More recently, Hightower et al. (2026preprint) suggested that gravimetric measurements may still be contaminated by solid-Earth viscous deformation signals that are not fully corrected by current GIA models. Such residual errors could lead to an underestimation of the ocean bottom pressure signal, particularly in the North Atlantic.

6 Discussion

This study presents an updated assessment of the global and regional sea-level budget over the satellite era, introducing refined uncertainty characterization and an objective inverse closure approach. Global mean sea-level rose at $3.39 \pm 0.20\ mm\ yr^{-1}$ since 1993 and accelerated to $3.86 \pm 0.18\ mm\ yr^{-1}$ over the GRACE/GRACE-FO period, driven primarily by land ice mass loss from glaciers, the Greenland Ice Sheet, and Antarctica, alongside a thermosteric contribution of approximately $1.3\ mm\ yr^{-1}$. The budget closes robustly until around 2015, after which a persistent and statistically significant residual trend emerges — present whether the barystatic component is drawn from GRACE/GRACE-FO gravimetry or from the sum of individual mass contributions — pointing to an inconsistency in the observing system or a missing contribution to the budget, rather than an artifact located in time of any single dataset.

A particularly striking result is that the ocean mass budget closes successfully until 2015 and then breaks down thereafter. This suggests the ocean mass estimate as a potential driver of the non-closure of the sea-level budget. Trend diagrams confirm that long-term residual trends of the sea-level budget are largely driven by episodic errors occurring near the end of the

https://doi.org/10.5194/essd-2026-627
Preprint. Discussion started: 19 August 2026

time series, which then propagate into trend estimates — particularly when the trend period starts or ends at those specific epochs. Artifacts can be identified indeed episodically around 2015 in the budget based on the sum of mass components, and around 2018 and 2020 in the budget based on satellite gravimetry potentially pointing at issues at these dates in GRACE-FO. Additionally, ENSO events exert a significant short-term and episodic influence on the sea-level budget closure, especially when individual mass components are used, highlighting persistent challenges in capturing the full amplitude of interannual signals — most likely linked to the land water storage component. Beyond these episodic effects, the SLB residuals consistently exhibit low-frequency variations that remain unexplained and may reflect inconsistencies across multiple components of the budget, not solely in the ocean mass term.

At the regional scale, the spatial structure of the residuals provides further diagnostic insight. Budget non-closure is concentrated in the North Atlantic and around Australia (with extensions into the Indian Ocean and and the south Pacific ocean), and to a lesser extent, in the North Pacific. Notably, this pattern of non-closure closely resembles the spatial pattern of the largest steric sea-level signals, suggesting that errors in temperature or salinity measurements may lead to an underestimation of the steric contribution. In the North Atlantic, the thermosteric and halosteric components exhibit a marked anti-correlation, consistent with density-compensated ("spice") anomalies driven by atmospheric forcing (for instance, through atmospheric modes like NAO, which simultaneously modulate heat fluxes and evaporation minus precipitation, producing correlated temperature and salinity anomalies that largely cancel in their density effect). Crucially, however, the residual pattern does not mirror this compensation pattern. This implies that the non-closure in this region cannot be attributed to errors in temperature or salinity measurements alone, since such errors would disrupt the density-neutral character of the observed steric anomaly. Instead, it points toward a systematic underestimation of the steric contribution as a whole — consistent with a missing deep-ocean component extending below 2000 m, beyond the reach of Argo floats as in Cazenave et al. (2026). A complementary explanation is that satellite altimetry overestimates the amplitude of regional sea-level signals; since regional sea-level patterns are largely dominated by steric variability, an overestimate in altimetry would produce residuals with a spatial structure similar to the steric signal itself. In summary, the classical budget approach points to three potential causes for the non-closure: (1) errors in the ocean mass component estimated from space gravimetry or the water budget, (2) a missing deep-ocean steric contribution as pointed out by Cazenave et al. (2026), and (3) an overestimation of sea-level by satellite altimetry.

To investigate these causes further, we implemented an objective weighted least-squares inversion. This approach could only be applied from 2004 onward, when both space gravimetry and Argo data are available and their uncertainties are sufficiently well characterized. The inversion demonstrates that an optimal closed solution exists within the combined uncertainties over 2004–2024. However, from 2017 onward, closure is not achieved within the 1σ uncertainty of the ocean mass estimate, meaning the budget closes with less than 32% probability since that date — indicating that a genuine inconsistency is more likely than not. Importantly, the objective method does not require significant adjustment to the satellite altimetry sea-level estimate, but proposes substantial corrections to the space gravimetry component, particularly after 2015. This again points toward space gravimetry as the most likely source of non-closure, coinciding with the GRACE to GRACE-FO mission transition and the ocean mass budget misclosure identified independently.

https://doi.org/10.5194/essd-2026-627
Preprint. Discussion started: 19 August 2026

To build on this finding, the objective approach should be extended to the regional scale, where it could help identify the geographic patterns underlying the global non-closure. This extension is currently limited by the absence of estimated spatial error correlations for each component, which means the inversion can only be performed independently at each grid cell.

7 Data availability

A compiled dataset of time series of the elements presented in this study is freely available for download at https://climate.esa.int/en/projects/sea-level-budget-closure/. The data are available in 2 separate netCDF files: (1) the GMSL budget and of the GWMB together with their uncertainties from direct approach at global and regional scales over period 1993-2022 and 2004-2022 respectively (presented in sections 4, 5.2 an 5.1.1); (2) the GMSL budget elements with their uncertainties from objective closure approach at global scale over period 2004-2022 (presented in section 5.1.2). These datasets are all at an identical monthly sampling, resulting from interpolation of the original time series where necessary. Uncertainties are delivered in the form of variance covariance matrices at yearly sampling. Seasonal signals are removed from all time series.

Author contributions. AB,BM,MA,MB,RFr and RFe designed the study. AB, BM, RFr, and MB led the study and the compilation and editing of the manuscript. MA,RFr, and MB contributed the GMSL dataset and its description. NK,WL, and EO contributed the steric dataset and its description. MH and TD contributed the gravimetry-based barystatic and manometric dataset and it description. JB and ID contributed the global glacier dataset and its description. MH and TD contributed the Greenland and Antartica mass change dataset and its description. GS and DM contributed to the GIA dataset and its description RFe,RFr, and MB contributed the LWS and Atmospheric water vapor datasets and their description. AB,BM,MA,MB,RFr and RFe conducted the global water and sea-level budgets analyses and drafted their description.

All authors discussed the results and contributed to the editing of the manuscript. RF managed the project administration. SC launched the ESA Sea Level Budget Closure CCI (SLBC_cci) project and supervised the development of this research activity and reviewed all the deliverables.

Competing interests. None

Acknowledgements. This study was supported by the European Space Agency through the Sea Level Budget Closure Climate Change Initiative (CCI) project

https://doi.org/10.5194/essd-2026-627
Preprint. Discussion started: 19 August 2026

Appendix A: Mathematical support for the objective approach apply to the SLB

Let us define the vector m of relative sea-level changes (computed as the difference between absolute sea-level changes and vertical land motion), barystatic contribution and thermosteric contribution:

$$\boldsymbol{m} = \begin{bmatrix} h_{rel}(1) \\ \vdots \\ h_{rel}(n_t) \\ h_B(1) \\ \vdots \\ h_B(n_t) \\ h_\theta(1) \\ \vdots \\ h_\theta(n_t) \end{bmatrix}$$

where n_t is the number of time samples. We denote by $\boldsymbol{m}_{\text{obs}}$ the vector of observed components and by $\boldsymbol{m}_{\text{est}}$ the vector containing the estimated components.

The error covariance matrix of the observed component vector $\mathbf{C}_{\text{obs}}$ is a $[3n_t, 3n_t]$ block diagonal matrix containing the $[n_t, n_t]$ error covariance matrices of each component on diagonal blocks:

$$\mathbf{C}_{\text{obs}} = \begin{bmatrix} \mathbf{C}_h & 0 & 0 \\ 0 & \mathbf{C}_{h_B} & 0 \\ 0 & 0 & \mathbf{C}_{h_\theta} \end{bmatrix}$$

.

We also define the vector of the global mean sea-level budget residuals as:

$$\boldsymbol{R} = \begin{bmatrix} R_1 \\ \vdots \\ R_{n_t} \end{bmatrix}$$

The component vector and the residual vector are linearly related via the Jacobian matrix $\mathbf{K}$ containing the derivatives of $\boldsymbol{R}$ with respect to $\boldsymbol{m}$:

$$\boldsymbol{R} = \mathbf{K}\boldsymbol{m}$$

where $\mathbf{K}$ is a $[n_t, n_t]$ matrix constructed as follows:

$$\mathbf{K} = \begin{bmatrix} \mathbf{I}_{n_t} & -\mathbf{I}_{n_t} & -\mathbf{I}_{n_t} \end{bmatrix}$$

with $\mathbf{I}_{n_t}$ being the identity matrix of dimension $[n_t, n_t]$. We define a cost function J which includes one term to minimize the likelihood of the components taking as weight their error covariance matrix and one term to minimize the residuals of the

https://doi.org/10.5194/essd-2026-627
Preprint. Discussion started: 19 August 2026

estimated components. This second term is the soft constraint that must equal zero to enforce closure of the sea-level budget:

$$J(\boldsymbol{m}) = ||\boldsymbol{m} - \boldsymbol{m}_{\text{obs}}||^2 + \alpha||\boldsymbol{R}||^2 = (\boldsymbol{m} - \boldsymbol{m}_{\text{obs}})^T \mathbf{C}_{\text{obs}} (\boldsymbol{m} - \boldsymbol{m}_{\text{obs}}) + \alpha(\mathbf{K}\boldsymbol{m})^T(\mathbf{K}\boldsymbol{m}) \tag{A1}$$

The scalar α in eq. A1 is a trade-off coefficient between the two terms to minimise. In the following, we arbitrarily consider $\alpha = 1$. The best estimate $\boldsymbol{m}_{\text{est}}$ minimising the cost function J is expressed as in Rodell et al. (2015):

$$\boldsymbol{m}_{\text{est}} = \boldsymbol{m}_{\text{obs}} - (\mathbf{K}^T\mathbf{K} + \mathbf{C}_{\text{obs}}^{-1})^{-1}\mathbf{K}^T\mathbf{K}\boldsymbol{m}_{\text{obs}} \tag{A2}$$

And its associated error covariance matrix is:

$$\mathbf{C}_{\text{est}} = (\mathbf{K}^T\mathbf{K} + \mathbf{C}_{\text{obs}}^{-1})^{-1} \tag{A3}$$

$\boldsymbol{m}_{\text{est}}$ provides an estimate of the sea-level components, optimally adjusted with their respective uncertainty to close the sea-level budget.

https://doi.org/10.5194/essd-2026-627
Preprint. Discussion started: 19 August 2026

Appendix B: Rates of geoid height due to elastic response

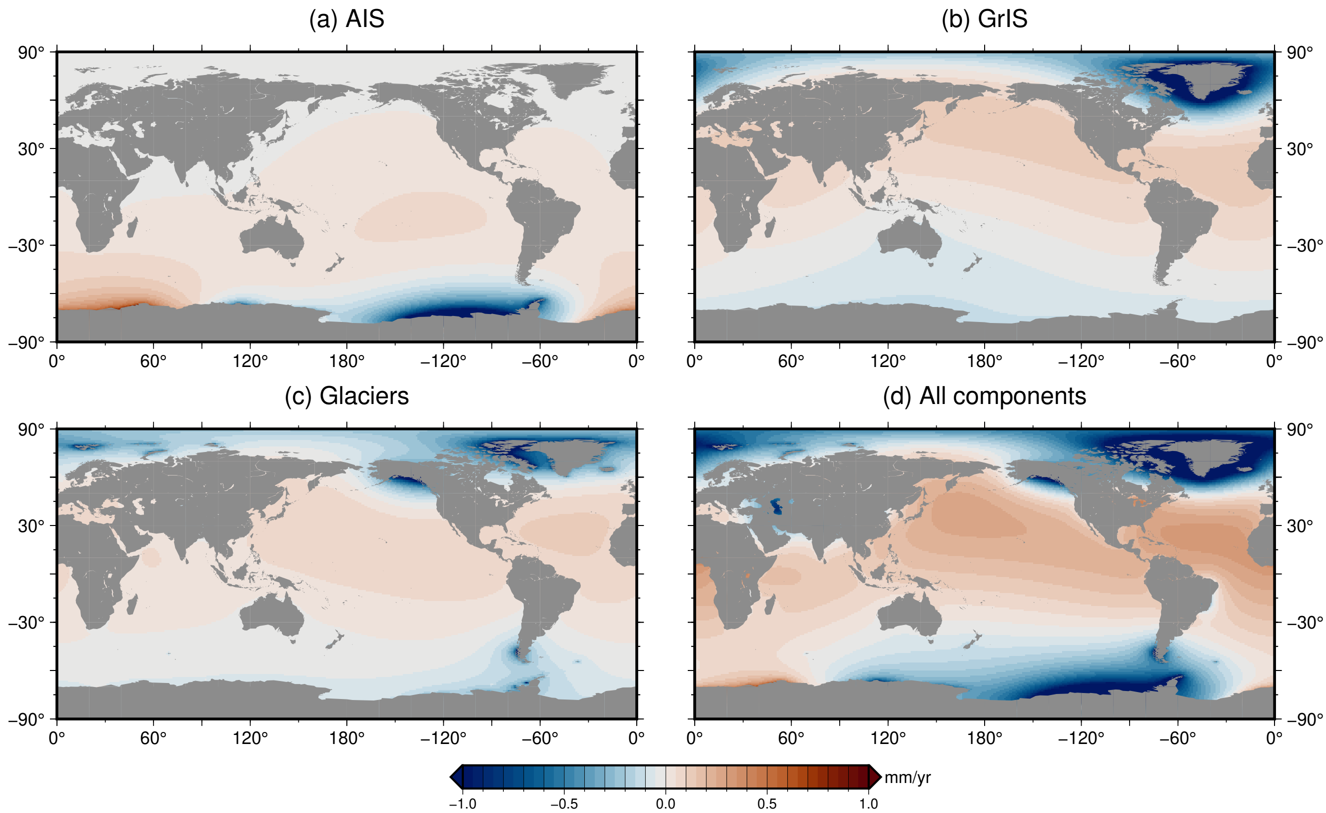

Figure B1. Average rates of geoid height change over 2002-2020 due to the elastic response of the Earth to redistribution of contemporary cryospheric and hydrological loads. Contributions due to the mass balance of Antarctic Ice Sheet (AIS, a), Greenland Ice Sheet (GrIS, b) and of glaciers and ice caps (c) are shown separately. Panel (d) shows the total response to the three mass components and to the variations in LWS.

https://doi.org/10.5194/essd-2026-627
Preprint. Discussion started: 19 August 2026

860 **Appendix C: Vertical correlation estimated from temperature**

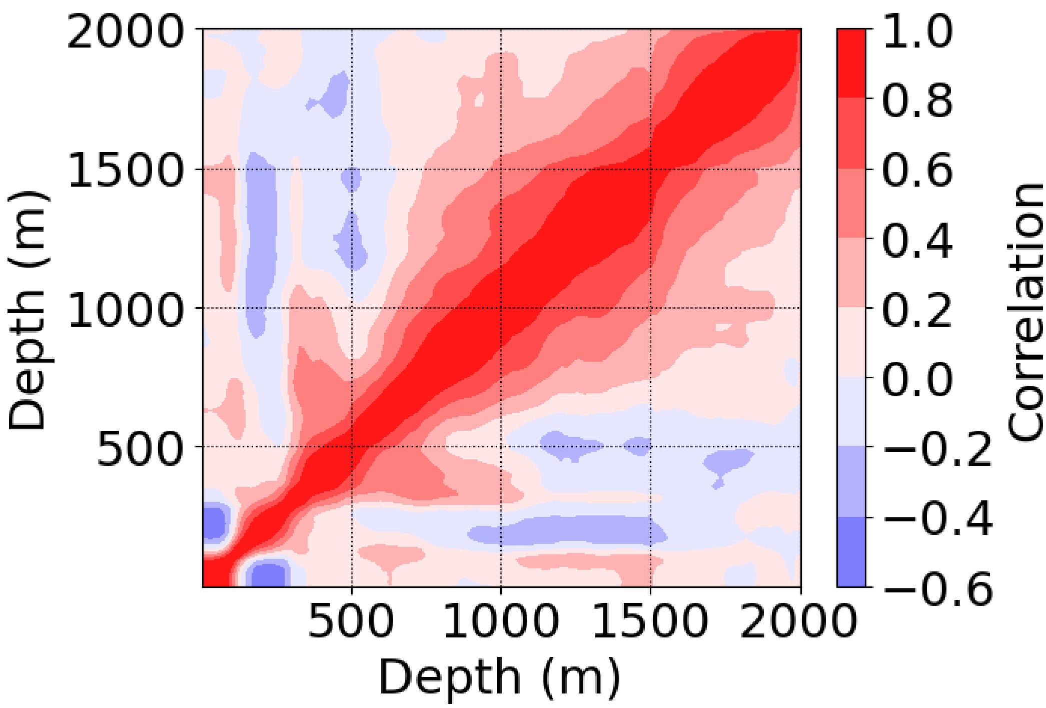

Figure C1. Vertical correlation matrix at 180°W and 1°S, estimated from temperature.

https://doi.org/10.5194/essd-2026-627
Preprint. Discussion started: 19 August 2026

Appendix D: Glacier and ice caps distribution

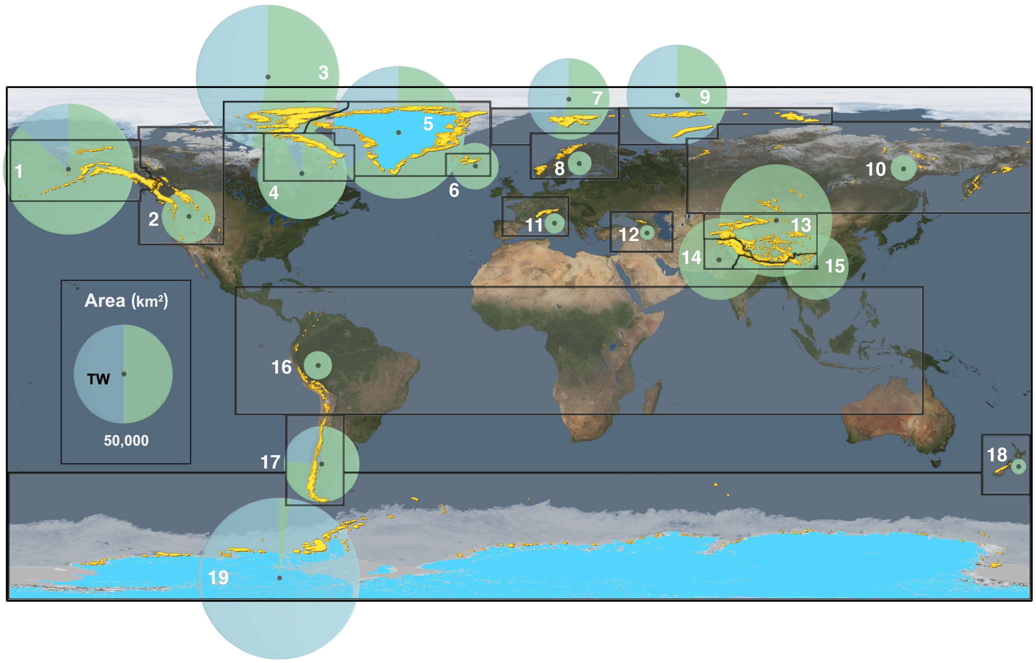

Figure D1. The 19 Glacier and Ice Cap regions used to estimate mass balance shown in yellow. The size of the circles indicates their area and the proportion shaded green or blue indicates the percentage area of land vs marine terminating glacier respectively. The light blue shading indicates the ice sheets.

https://doi.org/10.5194/essd-2026-627
Preprint. Discussion started: 19 August 2026

Appendix E: Global water budget residuals

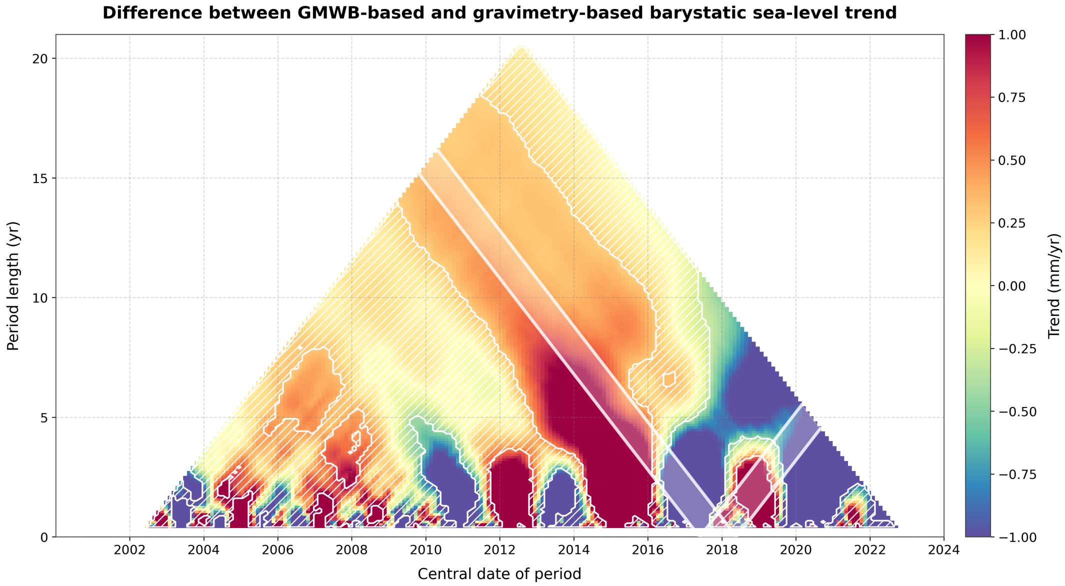

Figure E1. Pyramid trend diagram of the mass balance residuals (the difference between gravimetry-based and GWB-based barystatic) trend for any period and at any time. In dashed areas, the trend is not significant compared to its uncertainty.

Appendix F: Investigations on regional SLB misclosure

As discussed in the main text, the residual patterns around Australia closely resemble those of the thermosteric sea level, suggesting that the steric contribution may be underestimated in this region. By contrast, in the North Atlantic, the steric signal (computed as the sum of the thermosteric and halosteric components) does not exhibit spatial patterns consistent with the residuals, indicating that a different mechanism is likely responsible. This appendix provides additional analyses supporting these regional interpretations.

To further investigate the Australian residuals, we first tested the hypothesis of an underestimated steric contribution by applying a uniform scaling factor to the steric component and re-evaluating the sea level budget residuals (Figure F1). The results indicate that increasing the steric contribution by a factor of 1.3 substantially reduces the residuals over the Australian region, rendering most of them statistically insignificant with respect to their associated uncertainties. In contrast, the significant residual trend observed over the North Atlantic remains largely unchanged, further supporting the hypothesis that a different mechanism is responsible for the discrepancies in this region.

https://doi.org/10.5194/essd-2026-627
Preprint. Discussion started: 19 August 2026

Open Access Earth System Science Data Discussions

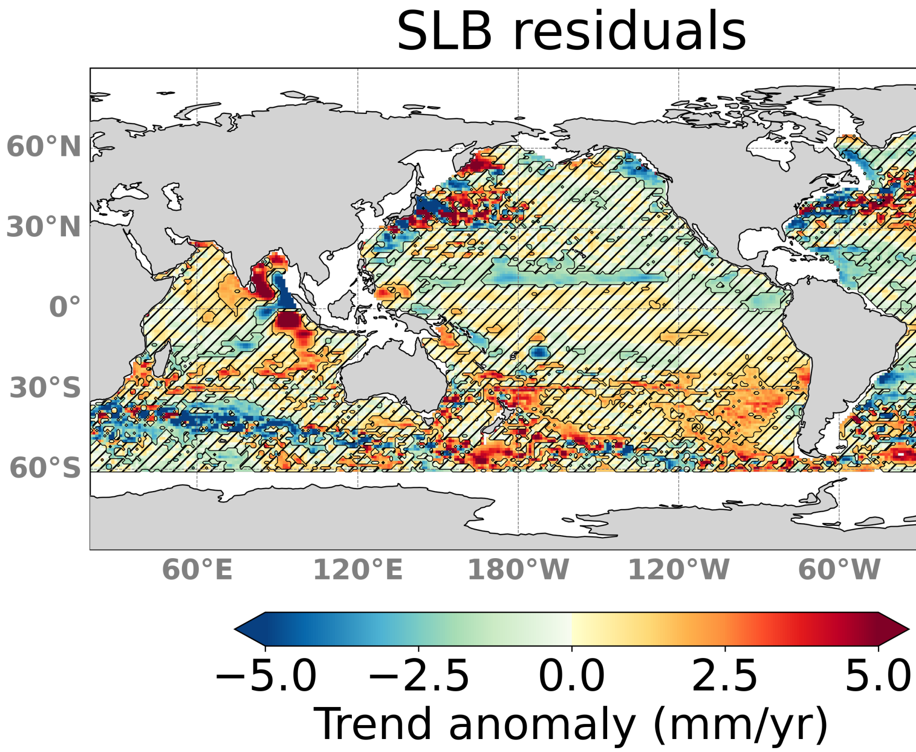

Figure F1. Budget residual trends over the period 2004-2022 by applying a factor of 1.3 on the steric component. In dashed areas, the trend is not significant compared with uncertainties.

Appendix G: Steric sea level

880 To complement the analysis of the individual components and further support the discussion, the total steric sea level trend anomaly map, computed as the spatial sum of the thermosteric and halosteric sea level contributions over the same period, is provided in Figure G1.

https://doi.org/10.5194/essd-2026-627
Preprint. Discussion started: 19 August 2026

Open Access Earth System Science Data Discussions

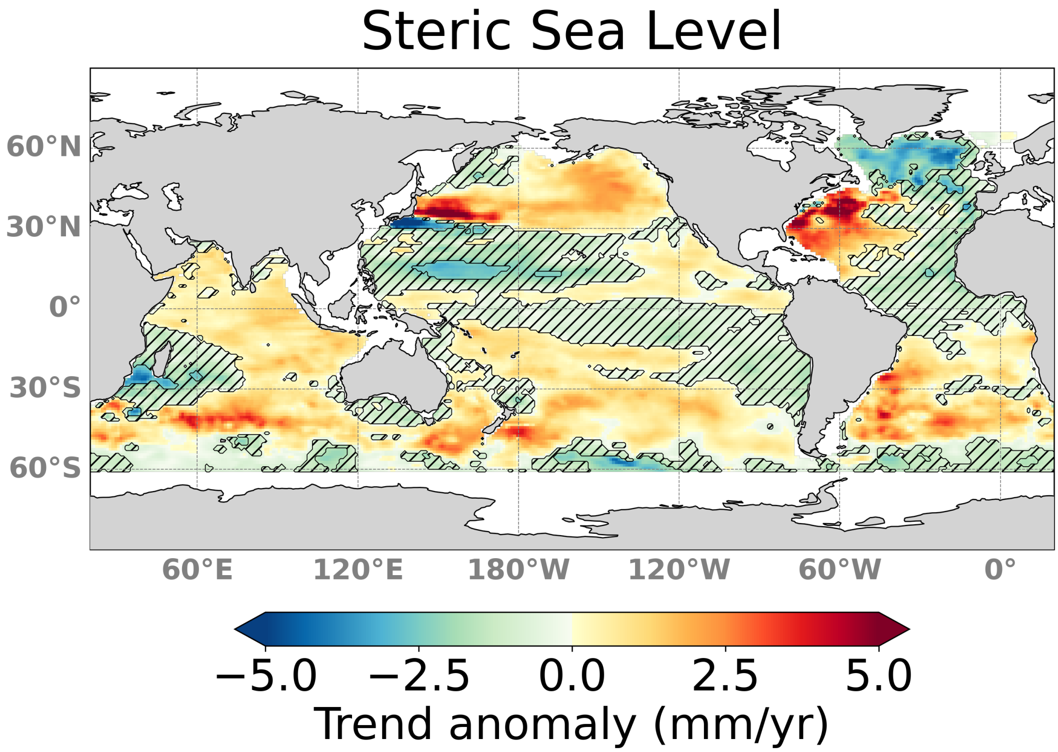

Figure G1. Steric sea level over the period 2004-2022. Dashed areas correspond where trends is not significant compared with uncertainties.

https://doi.org/10.5194/essd-2026-627
Preprint. Discussion started: 19 August 2026

Open Access Earth System Science Data Discussions

References

Ablain, M., Meyssignac, B., Zawadzki, L., Jugier, R., Ribes, A., Spada, G., Benveniste, J., Cazenave, A., and Picot, N.: Uncertainty in satellite estimates of global mean sea-level changes, trend and acceleration, Earth System Science Data, 11, 1189–1202, https://doi.org/10.5194/essd-11-1189-2019, 2019.

Argus, D. F., Peltier, W., Drummond, R., and Moore, A. W.: The Antarctica component of postglacial rebound model ICE-6G_C (VM5a) based on GPS positioning, exposure age dating of ice thicknesses, and relative sea level histories, Geophysical Journal International, 198, 537–563, 2014.

ATBD: Sea Level Budget Closure - Climate Change Initiative +, Algorithm Theoretical Baseline Document, https://climate.esa.int/media/documents/2024-10-31_SLBC_CCI-DT-041-MAG_ATBD_D2-4_V2_0_signed.pdf, 2025.

Bagnell, A. and DeVries, T.: Global Mean Sea Level Rise Inferred From Ocean Salinity and Temperature Changes, Geophysical Research Letters, 50, e2022GL101 004, https://doi.org/https://doi.org/10.1029/2022GL101004, 2023.

Barnoud, A., Pfeffer, J., Guérou, A., Frery, M., Siméon, M., Cazenave, A., Chen, J., Llovel, W., Thierry, V., Legeais, J., and Ablain, M.: Contributions of Altimetry and Argo to Non-Closure of the Global Mean Sea Level Budget Since 2016, Geophysical Research Letters, 48, e2021GL092 824, https://doi.org/10.1029/2021GL092824, 2021.

Barnoud, A., Bouih, M., Picard, B., Meyssignac, B., Marti, F., Ablain, M., and Roca, R.: Wet troposphere correction derived from water vapor climate data records, https://doi.org/10.24400/527896/A03-2023.3729, publisher: CNES, 2023a.

Barnoud, A., Pfeffer, J., Cazenave, A., Fraudeau, R., Rousseau, V., and Ablain, M.: Revisiting the global mean ocean mass budget over 2005–2020, Ocean Science, 19, 321–334, https://doi.org/10.5194/os-19-321-2023, 2023b.

Blazquez, A., Meyssignac, B., Lemoine, J.-M., Ribes, A., Berthier, E., and Cazenave, A.: Exploring the uncertainty in GRACE estimates of the mass redistributions at the Earth surface: Implications for the global water and sea level budgets, Geophysical Journal International, 215, 415–430, https://doi.org/10.1093/gji/ggy293, 2018.

Bouih, M., Barnoud, A., Yang, C., Storto, A., Blazquez, A., Llovel, W., Fraudeau, R., and Cazenave, A.: Regional sea level trend budget over 2004–2022, Ocean Science, 21, 1425–1440, https://doi.org/10.5194/os-21-1425-2025, 2025.

Brown, S., Willis, J., and Fournier, S.: Jason-3 Wet Path Delay Correction, https://doi.org/10.5067/J3L2G-PDCOR, 2023.

Cadier, E., Courcol, B., Prandi, P., Quet, V., Moreau, T., Maraldi, C., Bignalet-Cazalet, F., Dinardo, S., Martin-Puig, C., and Donlon, C.: Assessment of Sentinel-6MF low resolution numerical retracker over ocean: Continuity on reference orbit and improvements, Advances in Space Research, p. S0273117724011670, https://doi.org/10.1016/j.asr.2024.11.045, 2024.

Caron, L., Ivins, E. R., Larour, E., Adhikari, S., Nilsson, J., and Blewitt, G.: GIA Model Statistics for GRACE Hydrology, Cryosphere, and Ocean Science, Geophysical Research Letters, 45, 2203–2212, https://doi.org/10.1002/2017GL076644, 2018.

Cazenave, A. and Moreira, L.: Contemporary sea-level changes from global to local scales: a review, Proceedings of the Royal Society A: Mathematical, Physical and Engineering Sciences, 478, 20220 049, https://doi.org/10.1098/rspa.2022.0049, 2022.

Cazenave, A., Meyssignac, B., Ablain, M., Balmaseda, M., Bamber, J., Barletta, V., Beckley, B., Benveniste, J., Berthier, E., Blazquez, A., Boyer, T., Cáceres, D., Chambers, D., Champollion, N., Chao, B., Chen, J., Cheng, L., Church, J. A., Chuter, S., Cogley, J. G., Dangendorf, S., Desbruyères, D., Döll, P., Domingues, C., Falk, U., Famiglietti, J., Fenoglio-Marc, L., Forsberg, R., Galassi, G., Gardner, A., Groh, A., Hamlington, B., Hogg, A., Horwath, M., Humphrey, V., Husson, L., Ishii, M., Jäggi, A., Jevrejeva, S., Johnson, G. C., Kolodziejczyk, N., Kusche, J., Lambeck, K., Landerer, F., Leclercq, P. W., Legresy, B., Leuliette, E., Llovel, W., Longuevergne, L., Loomis, B. D., Luthcke, S. B., Marcos, M., Marzeion, B., Merchant, C., Merrifield, M., Milne, G., Mitchum, G., Mohajerani, Y., Monier, M., Monselesan, D.,

https://doi.org/10.5194/essd-2026-627
Preprint. Discussion started: 19 August 2026

Nerem, S., Palanisamy, H., Paul, F., Perez, B., Piecuch, C. G., Ponte, R. M., Purkey, S. G., Reager, J. T., Rietbroek, R., Rignot, E., Riva, R., Roemmich, D., Sørensen, L. S., Sasgen, I., Schrama, E., Seneviratne, S. I., Shum, C., Spada, G., Stammer, D., Velicogna, I., Von Schuckmann, K., Wada, Y., Wang, Y., Watson, C., Wiese, D., Wijffels, S., Westaway, R., Woppelmann, G., and Wouters, B.: Global sea-level budget 1993-present, https://doi.org/10.3929/ETHZ-B-000287786, medium: application/pdf, 2018.

Cazenave, A., Yang, C., Bouih, M., Storto, A., Chen, J., Llovel, W., von Schuckmann, K., and Leclercq, L.: Evidence of Increased Deep Ocean Warming From a Sea Level Budget Approach, Earth's Future, 14, e2025EF007 403, https://doi.org/10.1029/2025EF007403, 2026.

Chambers, D., Wahr, J., and Nerem, R. S.: Preliminary observations of global ocean mass variations with GRACE, Geophysical Research Letters, 31, L13 310, 2004.

Chen, J., Tapley, B., Wilson, C., Cazenave, A., Seo, K.-W., and Kim, J.-S.: Global Ocean Mass Change From GRACE and GRACE Follow-On and Altimeter and Argo Measurements, Geophysical Research Letters, 47, e2020GL090 656, https://doi.org/https://doi.org/10.1029/2020GL090656, _eprint: https://agupubs.onlinelibrary.wiley.com/doi/pdf/10.1029/2020GL090656, 2020.

Cheng, L. and Zhu, J.: Benefits of CMIP5 Multimodel Ensemble in Reconstructing Historical Ocean Subsurface Temperature Variations, Journal of Climate, 29, 5393 – 5416, https://doi.org/10.1175/JCLI-D-15-0730.1, 2016.

Cheng, L., Zhu, J., Cowley, R., Boyer, T., and Wijffels, S.: Time, probe type, and temperature variable bias corrections to historical expendable bathythermograph observations, Journal of Atmospheric and Oceanic Technology, 31, 1793–1825, 2014.

Church, J. A. and White, N. J.: A 20th century acceleration in global sea-level rise, Geophysical Research Letters, 33, 2005GL024 826, https://doi.org/10.1029/2005GL024826, 2006.

Copernicus Climate Change Service, C. D. S.: Sea level daily gridded data from satellite observations for the global ocean from 1993 to present, https://doi.org/10.24381/CDS.4C328C78, 2018.

Croteau, M. J., Sabaka, T. J., and Loomis, B. D.: GRACE Fast Mascons From Spherical Harmonics and a Regularization Design Trade Study, Journal of Geophysical Research: Solid Earth, 126, e2021JB022 113, https://doi.org/10.1029/2021JB022113, 2021.

Cáceres, D., Marzeion, B., Malles, J. H., Gutknecht, B. D., Müller Schmied, H., and Döll, P.: Assessing global water mass transfers from continents to oceans over the period 1948–2016, Hydrology and Earth System Sciences, 24, 4831–4851, https://doi.org/10.5194/hess-24-4831-2020, publisher: Copernicus GmbH, 2020.

Decharme, B., Delire, C., Minvielle, M., Colin, J., Vergnes, J.-P., Alias, A., Saint-Martin, D., Séférian, R., Sénési, S., and Voldoire, A.: Recent Changes in the ISBA-CTRIP Land Surface System for Use in the CNRM-CM6 Climate Model and in Global Off-Line Hydrological Applications, Journal of Advances in Modeling Earth Systems, 11, 1207–1252, https://doi.org/https://doi.org/10.1029/2018MS001545, 2019.

Dieng, H. B., Cazenave, A., Meyssignac, B., and Ablain, M.: New estimate of the current rate of sea level rise from a sea level budget approach, Geophysical Research Letters, 44, 3744–3751, https://doi.org/10.1002/2017gl073308, publisher: American Geophysical Union (AGU), 2017.

Ditmar, P.: How to quantify the accuracy of mass anomaly time-series based on GRACE data in the absence of knowledge about true signal?, Journal of Geodesy, 96, https://doi.org/10.1007/s00190-022-01697-8, 2022.

Dussaillant, I., Hugonnet, R., Huss, M., Berthier, E., Bannwart, J., Paul, F., and Zemp, M.: Annual mass changes for each glacier in the world from 1976 to 2023, Earth System Science Data Discussions, pp. 1–41, https://doi.org/10.5194/essd-2024-323, 2024.

Döhne, T., Horwath, M., Groh, A., and Buchta, E.: The sensitivity kernel perspective on GRACE mass change estimates, Journal of Geodesy, 97, 11–20, https://doi.org/10.1007/s00190-022-01697-8, 2023.

https://doi.org/10.5194/essd-2026-627
Preprint. Discussion started: 19 August 2026

Farrell, W. and Clark, J.: On Postglacial Sea Level, Geophysical Journal of the Royal Astronomical Society, 46, 647–667, https://doi.org/10.1111/j.1365-246X.1976.tb01252.x, 1976.

Gaillard, F., Reynaud, T., Thierry, V., and Kolodziejczyk, N.: In-situ based reanalysis of the global ocean temperature and salinity with ISAS: variability of the heat content and steric height, Journal Of Climate, 29, 1305–1323, https://doi.org/10.1175/JCLI-D-15-0028.1, 2016.

Good, S. A., Martin, M. J., and Rayner, N. A.: EN4: Quality controlled ocean temperature and salinity profiles and monthly objective analyses with uncertainty estimates, Journal of Geophysical Research: Oceans, 118, 6704–6716, https://doi.org/https://doi.org/10.1002/2013JC009067, 2013.

Gregory, J. M., Griffies, S. M., Hughes, C. W., Lowe, J. A., Church, J. A., Fukimori, I., Gomez, N., Kopp, R. E., Landerer, F., Cozannet, G. L., Ponte, R. M., Stammer, D., Tamisiea, M. E., and van de Wal, R. S. W.: Concepts and Terminology for Sea Level: Mean, Variability and Change, Both Local and Global, 40, 1251–1289, https://doi.org/10.1007/s10712-019-09525-z, 2019.

Groh, A. and Horwath, M.: Antarctic Ice Mass Change Products from GRACE/GRACE-FO Using Tailored Sensitivity Kernels, Remote Sensing, 13, 1736, https://doi.org/10.3390/rs13091736, 2021.

Guérou, A., Meyssignac, B., Prandi, P., Ablain, M., Ribes, A., and Bignalet-Cazalet, F.: Current observed global mean sea level rise and acceleration estimated from satellite altimetry and the associated measurement uncertainty, Ocean Science, 19, 431–451, https://doi.org/10.5194/os-19-431-2023, 2023.

Hakuba, M. Z., Fourest, S., Boyer, T., Meyssignac, B., Carton, J. A., Forget, G., Cheng, L., Giglio, D., Johnson, G. C., Kato, S., Killick, R. E., Kolodziejczyk, N., Kuusela, M., Landerer, F., Llovel, W., Locarnini, R., Loeb, N., Lyman, J. M., Mishonov, A., Pilewskie, P., Reagan, J., Storto, A., Sukianto, T., and Von Schuckmann, K.: Trends and Variability in Earth's Energy Imbalance and Ocean Heat Uptake Since 2005, Surveys in Geophysics, https://doi.org/10.1007/s10712-024-09849-5, 2024.

Hamlington, B. D., Gardner, A. S., Ivins, E., Lenaerts, J. T. M., Reager, J. T., Trossman, D. S., Zaron, E. D., Adhikari, S., Arendt, A., Aschwanden, A., Beckley, B. D., Bekaert, D. P. S., Blewitt, G., Caron, L., Chambers, D. P., Chandanpurkar, H. A., Christianson, K., Csatho, B., Cullather, R. I., DeConto, R. M., Fasullo, J. T., Frederikse, T., Freymueller, J. T., Gilford, D. M., Girotto, M., Hammond, W. C., Hock, R., Holschuh, N., Kopp, R. E., Landerer, F., Larour, E., Menemenlis, D., Merrifield, M., Mitrovica, J. X., Nerem, R. S., Nias, I. J., Nieves, V., Nowicki, S., Pangaluru, K., Piecuch, C. G., Ray, R. D., Rounce, D. R., Schlegel, N.-J., Seroussi, H., Shirzaei, M., Sweet, W. V., Velicogna, I., Vinogradova, N., Wahl, T., Wiese, D. N., and Willis, M. J.: Understanding of Contemporary Regional Sea-Level Change and the Implications for the Future, Reviews of Geophysics, 58, e2019RG000 672, https://doi.org/10.1029/2019RG000672, _eprint: https://agupubs.onlinelibrary.wiley.com/doi/pdf/10.1029/2019RG000672, 2020.

Hersbach, H., Comyn-Platt, E., Bell, B., Berrisford, P., Biavati, G., Horanyi, A., Munoz Sabater, J., Nicolas, J., Peubey, C., Radu, R., Rozum, I., Schepers, D., Simmons, A., Soci, C., Dee, D., Thépaut, J., Cagnazzo, C., and Cucchi, M.: ERA5 post-processed daily-statistics on pressure levels from 1940 to present, https://doi.org/https://doi.org/10.24381/cds.4991cf48, 2023.

Hightower, E., Caron, L., Landerer, F., Watkins, M., Ivins, E., and Larour, E.: Impact of Heterogeneous Mantle Viscosity on the Glacial Isostatic Adjustment Correction for GRACE(-FO): Implications for Surface Mass Trends, https://doi.org/10.22541/essoar.15004543/v1, 2026preprint.

Horwath, M., Gutknecht, B. D., Cazenave, A., Palanisamy, H. K., Marti, F., Marzeion, B., Paul, F., Bris, R. L., Hogg, A. E., Otosaka, I., Shepherd, A., Döll, P., Cáceres, D., Schmied, H. M., Johannessen, J. A., Nilsen, J. E. O., Raj, R. P., Forsberg, R., Sorensen, L. S., Barletta, V. R., Simonsen, S. B., Knudsen, P., Andersen, O. B., Randall, H., Rose, S. K., Merchant, C. J., Macintosh, C. R., Schuckmann, K. v., Novotny, K., Groh, A., Restano, M., and Benveniste, J.: Global sea-level budget and ocean-mass budget, with focus on advanced data products and uncertainty characterisation, 14, 411–447, https://doi.org/10.5194/essd-14-411-2022, publisher: Copernicus GmbH, 2022.

Hosoda, S., Ohira, T., and Nakamura, T.: A monthly mean dataset of global oceanic temperature and salinity derived from Argo float observations, JAMSTEC Report of Research and Development, 8, 47–59, https://doi.org/10.5918/jamstecr.8.47, 2008.

Hugonnet, R., McNabb, R., Berthier, E., Menounos, B., Nuth, C., Girod, L., Farinotti, D., Huss, M., Dussaillant, I., Brun, F., and Kääb, A.: Accelerated global glacier mass loss in the early twenty-first century, Nature, 592, 726–731, https://doi.org/10.1038/s41586-021-03436-z, 2021.

Humphrey, V. and Gudmundsson, L.: GRACE-REC: a reconstruction of climate-driven water storage changes over the last century, 11, 1153–1170, https://doi.org/10.5194/essd-11-1153-2019, 2019.

Ishii, M., Kimoto, M., and Kachi, M.: Historical ocean subsurface temperature analysis with error estimates, Monthly Weather Review, 131, 51–73, 2003.

Ishii, M., Kimoto, M., Sakamoto, K., and Iwasaki, S.-I.: Steric sea level changes estimated from historical ocean subsurface temperature and salinity analyses, Journal of Oceanography, 62, 155–170, https://doi.org/10.1007/s10872-006-0041-y, 2006.

Ivins, E. R., James, T. S., Wahr, J., Schrama, E. J. O., Landerer, F. W., and Simon, K. M.: Antarctic contribution to sea level rise observed by GRACE with improved GIA correction, Journal of Geophysical Research: Solid Earth, 118, 3126–3141, https://doi.org/10.1002/jgrb.50208, 2013.

Kolodziejczyk, N., Prigent-Mazella, A., and Gaillard, F.: ISAS temperature, salinity, dissolved oxygen gridded fields, https://doi.org/10.17882/52367, 2023.

Kustowski, B., Ekström, G., and Dziewonski, A.: Anisotropic shear-wave velocity structure of the Earth's mantle: A global model, Journal of Geophysical Research: Solid Earth, 113, 2008.

Kvas, A., Behzadpour, S., Ellmer, M., Klinger, B., Strasser, S., Zehentner, N., and Mayer-Gürr, T.: ITSG-Grace2018: Overview and Evaluation of a New GRACE-Only Gravity Field Time Series, Journal of Geophysical Research: Solid Earth, 124, 9332–9344, https://doi.org/10.1029/2019JB017415, 2019.

Landerer, F. W., Flechtner, F. M., Save, H., Webb, F. H., Bandikova, T., Bertiger, W. I., Bettadpur, S. V., Byun, S. H., Dahle, C., Dobslaw, H., Fahnestock, E., Harvey, N., Kang, Z., Kruizinga, G. L. H., Loomis, B. D., McCullough, C., Murböck, M., Nagel, P., Paik, M., Pie, N., Poole, S., Strekalov, D., Tamisiea, M. E., Wang, F., Watkins, M. M., Wen, H.-Y., Wiese, D. N., and Yuan, D.-N.: Extending the Global Mass Change Data Record: GRACE Follow-On Instrument and Science Data Performance, Geophysical Research Letters, 47, e2020GL088 306, https://doi.org/https://doi.org/10.1029/2020GL088306, _eprint: https://agupubs.onlinelibrary.wiley.com/doi/pdf/10.1029/2020GL088306, 2020.

Leclercq, L., Dieng, H. B., Cazenave, A., Birol, F., Oelsmann, J., Passaro, M., Jevrejeva, S., Bergsma, E., and Connors, S.: Spatio-temporal changes in interannual sea level along the world coastlines, Global and Planetary Change, 253, 104 972, https://doi.org/10.1016/j.gloplacha.2025.104972, 2025.

Levitus, S., Antonov, J. I., Boyer, T. P., Locarnini, R. A., Garcia, H. E., and Mishonov, A. V.: Global ocean heat content 1955–2008 in light of recently revealed instrumentation problems, Geophysical Research Letters, 36, https://doi.org/https://doi.org/10.1029/2008GL037155, 2009.

Liu, C., Liang, X., Ponte, R. M., and Chambers, D. P.: "Salty Drift" of argo floats affects the gridded ocean salinity products, Journal of Geophysical Research: Oceans, 129, 2024.

Loomis, B. D., Luthcke, S. B., and Sabaka, T. J.: Regularization and error characterization of GRACE mascons, Journal of Geodesy, 93, 1381–1398, https://doi.org/10.1007/s00190-019-01252-y, 2019.

https://doi.org/10.5194/essd-2026-627
Preprint. Discussion started: 19 August 2026

Loomis, B. D., Sabaka, T. J., Rachlin, K. E., Croteau, M. J., Lemoine, F. G., Nerem, R. S., and Bellas-Manley, A.: Optimized J2 Recovery for Multi-Decadal Geophysical Studies, Geophysical Research Letters, 52, e2024GL114 472, https://doi.org/10.1029/2024GL114472, 2025.

Meyer, U., Lasser, M., Dahle, C., Förste, C., Behzadpour, S., Koch, I., and Jäggi, A.: Combined Monthly GRACE-FO Gravity Fields for a Global Gravity-Based Groundwater Product, Geophysical Journal International, 236, 456–469, https://doi.org/10.1093/gji/ggad437, 2024.

Mitrovica, J. X., Wahr, J., Matsuyama, I., and Paulson, A.: The rotational stability of an ice-age earth, Geophysical Journal International, 161, 491–506, 2005.

Moreira, L., Cazenave, A., Barnoud, A., and Chen, J.: Sea-Level Fingerprints Due to Present-Day Water Mass Redistribution in Observed Sea-Level Data, Remote Sensing, 13, 4667, https://doi.org/10.3390/rs13224667, 2021.

Munk, W. and Revelle, R.: Sea level and the rotation of the Earth, American Journal of Science, pp. 829–833, 1952.

Müller Schmied, H., Cáceres, D., Eisner, S., Flörke, M., Herbert, C., Niemann, C., Peiris, T. A., Popat, E., Portmann, F. T., Reinecke, R., Schumacher, M., Shadkam, S., Telteu, C.-E., Trautmann, T., and Döll, P.: The global water resources and use model WaterGAP v2.2d: model description and evaluation, 14, 1037–1079, https://doi.org/10.5194/gmd-14-1037-2021, 2021.

Müller Schmied, H., Trautmann, T., Ackermann, S., Cáceres, D., Flörke, M., Gerdener, H., Kynast, E., Peiris, T. A., Schiebener, L., Schumacher, M., and Döll, P.: The global water resources and use model WaterGAP v2.2e: description and evaluation of modifications and new features, Geoscientific Model Development, 17, 8817–8852, https://doi.org/10.5194/gmd-17-8817-2024, 2024.

Nerem, R. S., Chambers, D. P., Choe, C., and Mitchum, G. T.: Estimating Mean Sea Level Change from the TOPEX and Jason Altimeter Missions, Marine Geodesy, 33, 435–446, https://doi.org/10.1080/01490419.2010.491031, 2010.

Otosaka, I. N., Shepherd, A., Ivins, E. R., Schlegel, N.-J., Amory, C., van den Broeke, M. R., Horwath, M., Joughin, I., King, M. D., Krinner, G., Nowicki, S., Payne, A. J., Rignot, E., Scambos, T., Simon, K. M., Smith, B. E., Sørensen, L. S., Velicogna, I., Whitehouse, P. L., Geruo, A., Agosta, C., Ahlstrøm, A. P., Blazquez, A., Colgan, W., Engdahl, M. E., Fettweis, X., Forsberg, R., Gallée, H., Gardner, A., Gilbert, L., Gourmelen, N., Groh, A., Gunter, B. C., Harig, C., Helm, V., Khan, S. A., Kittel, C., Konrad, H., Langen, P. L., Lecavalier, B. S., Liang, C.-C., Loomis, B. D., McMillan, M., Melini, D., Mernild, S. H., Mottram, R., Mouginot, J., Nilsson, J., Noël, B., Pattle, M. E., Peltier, W. R., Pie, N., Roca, M., Sasgen, I., Save, H. V., Seo, K.-W., Scheuchl, B., Schrama, E. J. O., Schröder, L., Simonsen, S. B., Slater, T., Spada, G., Sutterley, T. C., Vishwakarma, B. D., van Wessem, J. M., Wiese, D., van der Wal, W., and Wouters, B.: Mass balance of the Greenland and Antarctic ice sheets from 1992 to 2020, Earth System Science Data, 15, 1597–1616, https://doi.org/10.5194/essd-15-1597-2023, 2023.

Peltier, W., Argus, D., and Drummond, R.: Space geodesy constrains ice age terminal deglaciation: The global ICE-6G_C (VM5a) model, Journal of Geophysical Research: Solid Earth, 120, 450–487, 2015.

Ponte, R., Sun, Q., Liu, C., and Liang, X.: How Salty Is the Global Ocean: Weighing It All or Tasting It a Sip at a Time?, Geophysical Research Letters, 48, https://doi.org/10.1029/2021GL092935, 2021.

Prandi, P., Meyssignac, B., Ablain, M., Spada, G., and Ribes, A.: Error variance-covariance, trends, accelerations and uncertainties of regional mean sea level estimated from satellite altimetry, https://doi.org/10.17882/74862, 2020.

Prandi, P., Meyssignac, B., Ablain, M., Spada, G., Ribes, A., and Benveniste, J.: Local sea level trends, accelerations and uncertainties over 1993–2019, Scientific Data, 8, 1, https://doi.org/10.1038/s41597-020-00786-7, 2021.

Purkey, S. and Johnson, G.: Warming of Global Abyssal and Deep Southern Ocean Waters Between the 1990s and 2000s: Contributions to Global Heat and Sea Level Rise Budgets *, Bldg, 3, https://doi.org/10.1175/2010JCLI3682.1, 2010.

RGI 7.0 Consortium: Randolph Glacier Inventory - A Dataset of Global Glacier Outlines, Version 7.0., NSIDC: National Snow and Ice Data Center, https://doi.org/doi:10.5067/f6jmovy5navz, 2023.

https://doi.org/10.5194/essd-2026-627
Preprint. Discussion started: 19 August 2026

Rietbroek, R., Brunnabend, S.-E., Kusche, J., Schröter, J., and Dahle, C.: Revisiting the contemporary sea-level budget on global and regional scales, Proceedings of the National Academy of Sciences, 113, 1504–1509, https://doi.org/10.1073/pnas.1519132113, 2016.

Rodell, M., Beaudoing, H., L'Ecuyer, T., Olson, W., Famiglietti, J., Houser, P., Adler, R., Bosilovich, M., Clayson, C., Chambers, D., Clark, E., Fetzer, E., Gu, G., Hilburn, K., Huffman, G., Lettenmaier, D., Liu, W. T. L., Robertson, F., Sheffield, J., and Gao, X.: The Observed State of the Water Cycle in the Early Twenty-First Century, 2015.

Roemmich, D. and Gilson, J.: The 2004–2008 mean and annual cycle of temperature, salinity, and steric height in the global ocean from the Argo Program, Progress in Oceanography, 82, 81–100, https://doi.org/https://doi.org/10.1016/j.pocean.2009.03.004, 2009.

Roquet, F., Madec, G., McDougall, T. J., and Barker, P. M.: Accurate polynomial expressions for the density and specific volume of seawater using the TEOS-10 standard, Ocean Modelling, 90, 29–43, https://doi.org/10.1016/j.ocemod.2015.04.002, 2015.

Rounce, D. R., Hock, R., Prusevich, A. A., Grogan, D. S., Lammers, R. B., Huss, M., Bliss, A., and Zan, B.: Downstream Hydrology Reduces Glaciers' Direct Contribution to Sea-Level Rise, Geophysical Research Letters, 52, e2025GL114 866, https://doi.org/10.1029/2025GL114866, _eprint: https://agupubs.onlinelibrary.wiley.com/doi/pdf/10.1029/2025GL114866, 2025.

Roy, K. and Peltier, W.: Glacial isostatic adjustment, relative sea level history and mantle viscosity: reconciling relative sea level model predictions for the U.S. East coast with geological constraints, Geophysical Journal International, 201, 1156–1181, https://doi.org/10.1093/gji/ggv066, 2015.

Santoso, A., McPhaden, M. J., and Cai, W.: The Defining Characteristics of ENSO Extremes and the Strong 2015/2016 El Niño, Reviews of Geophysics, 55, 1079–1129, https://doi.org/10.1002/2017RG000560, 2017.

Save, H., Bettadpur, S., and Tapley, B. D.: High-resolution CSR GRACE RL05 mascons, Journal of Geophysical Research: Solid Earth, 121, 7547–7569, https://doi.org/10.1002/2016jb013007, 2016.

Song, Z., Cazenave, A., Llovel, W., Storto, A., and Bouih, M.: North Atlantic sea level budget revisited, EGUsphere, 2026, 1–39, https://doi.org/10.5194/egusphere-2026-802, preprint.

Spada, G. and Melini, D.: SELEN^{4} (SELEN version 4.0): a Fortran program for solving the gravitationally and topographically self-consistent sea-level equation in glacial isostatic adjustment modeling, Geoscientific Model Development, 12, 5055–5075, https://doi.org/10.5194/gmd-12-5055-2019, 2019.

Spada, G. and Melini, D.: Glacial Isostatic Adjustment, Springer, 2025.

Stammer, D., Ray, R. D., Andersen, O. B., Arbic, B. K., Bosch, W., Carrère, L., Cheng, Y., Chinn, D. S., Dushaw, B. D., Egbert, G. D., Erofeeva, S. Y., Fok, H. S., Green, J. A. M., Griffiths, S., King, M. A., Lapin, V., Lemoine, F. G., Luthcke, S. B., Lyard, F., Morison, J., Müller, M., Padman, L., Richman, J. G., Shriver, J. F., Shum, C. K., Taguchi, E., and Yi, Y.: Accuracy assessment of global barotropic ocean tide models, Reviews of Geophysics, 52, 243–282, https://doi.org/10.1002/2014RG000450, 2014.

Stephens, G., Polcher, J., Zeng, X., Oevelen, P. v., Poveda, G., Bosilovich, M., Ahn, M.-H., Balsamo, G., Duan, Q., Hegerl, G., Jakob, C., Lamptey, B., Leung, R., Piles, M., Su, Z., Dirmeyer, P., Findell, K. L., Verhoef, A., Ek, M., L'Ecuyer, T., Roca, R., Nazemi, A., Dominguez, F., Klocke, D., and Bony, S.: The First 30 Years of GEWEX, Bulletin of the American Meteorological Society, 104, E126–E157, https://doi.org/10.1175/BAMS-D-22-0061.1, 2023.

Sun, Y., Riva, R. E. M., and Ditmar, P.: Optimizing Estimates of Annual Variations and Trends in Geocenter Motion and J2 from a Combination of GRACE Data and Geophysical Models, Journal of Geophysical Research: Solid Earth, 121, 8352–8370, https://doi.org/10.1002/2016JB013073, 2016.

Swenson, S., Chambers, D. P., and Wahr, J.: Estimating Geocenter Variations from a Combination of GRACE and Ocean Model Output, Journal of Geophysical Research: Solid Earth, 113, B08 410, https://doi.org/10.1029/2007JB005338, 2008.

https://doi.org/10.5194/essd-2026-627
Preprint. Discussion started: 19 August 2026

Tamisiea, M. E.: Ongoing glacial isostatic contributions to observations of sea level change, Geophysical Journal International, 186, 1036–1044, 2011.

Tapley, B. D., Bettadpur, S., Ries, J. C., Thompson, P. F., and Watkins, M. M.: GRACE Measurements of Mass Variability in the Earth System, Science, 305, 503–505, https://doi.org/10.1126/science.1099192, 2004.

Tegmark, M.: An icosahedron-based method for pixelizing the celestial sphere, The Astrophysical Journal, 470, L81, 1996.

UCR: Sea Level Budget Closure - Climate Change Initiative +, Uncertainty Characterisation Report, https://climate.esa.int/media/documents/2025-03-31_SLBC_CCI-DT-076-MAG_UCR_D3-5_V1_0-SIGNED.pdf, 2025.

Uebbing, B., Kusche, J., Rietbroek, R., and Landerer, F. W.: Processing Choices Affect Ocean Mass Estimates From GRACE, Journal of Geophysical Research: Oceans, 124, 1029–1044, https://doi.org/10.1029/2018JC014341, 2019.

University of Colorado Sea Level Research Group: Global Mean Sea Level Time Series, Release 2026rel1-0, https://sealevel.colorado.edu/data/2026rel1-0, accessed: [2026-07-07], 2026.

von Schuckmann, K., Gaillard, F., and Le Traon, P.-Y.: Global hydrographic variability patterns during 2003–2008, Journal of Geophysical Research: Oceans, 114, https://doi.org/https://doi.org/10.1029/2008JC005237, 2009.

Warrick, R. and Oerlemans, J.: Sea level rise, https://dspace.library.uu.nl/items/342ef8b9-8f1c-4095-bc30-ba659a3411a5, 1990.

WCRP Global Sea Level Budget Group: Global sea-level budget 1993–present, Earth System Science Data, 10, 1551–1590, https://doi.org/10.5194/essd-10-1551-2018, 2018.

Wiese, D. N., Landerer, F. W., and Watkins, M. M.: Quantifying and reducing leakage errors in the JPL RL05M GRACE mascon solution, Water Resources Research, 52, 7490–7502, https://doi.org/10.1002/2016WR019344, 2016.

Wong, A. P. S., Gilson, J., and Cabanes, C.: Argo salinity: bias and uncertainty evaluation, Earth System Science Data, 15, 383–393, https://doi.org/10.5194/essd-15-383-2023, 2023.

Zemp, M., Jakob, L., Dussaillant, I., Nussbaumer, S. U., Gourmelen, N., Dubber, S., A, G., Abdullahi, S., Andreassen, L. M., Berthier, E., Bhattacharya, A., Blazquez, A., Boehm Vock, L. F., Bolch, T., Box, J., Braun, M. H., Brun, F., Cicero, E., Colgan, W., Eckert, N., Farinotti, D., Florentine, C., Floricioiu, D., Gardner, A., Harig, C., Hassan, J., Hugonnet, R., Huss, M., Jóhannesson, T., Liang, C.-C. A., Ke, C.-Q., Khan, S. A., King, O., Kneib, M., Krieger, L., Maussion, F., Mattea, E., McNabb, R., Menounos, B., Miles, E., Moholdt, G., Nilsson, J., Pálsson, F., Pfeffer, J., Piermattei, L., Plummer, S., Richter, A., Sasgen, I., Schuster, L., Seehaus, T., Shen, X., Sommer, C., Sutterley, T., Treichler, D., Velicogna, I., Wouters, B., Zekollari, H., Zheng, W., and The GlaMBIE Team: Community estimate of global glacier mass changes from 2000 to 2023, Nature, 639, 382–388, https://doi.org/10.1038/s41586-024-08545-z, 2025.